

The vibronic level structure of the cyclopentadienyl radical

Takatoshi Ichino,^{1,2} Scott W. Wren,¹ Kristen M. Vogelhuber,¹ Adam J. Gianola,¹ W. Carl Lineberger,^{1,a),b)} and John F. Stanton^{3,a),c)}

¹*JILA and Department of Chemistry and Biochemistry, University of Colorado, Boulder, Colorado 80309-0440, USA*

²*Department of Chemistry and Biochemistry, The University of Texas at Austin, Austin, Texas 78712-0165, USA*

³*Institute for Theoretical Chemistry and Department of Chemistry and Biochemistry, The University of Texas at Austin, Austin, Texas 78712-0165, USA*

(Received 23 May 2008; accepted 28 July 2008; published online 28 August 2008)

The 351.1 nm photoelectron spectrum of the cyclopentadienide ion has been measured, which reveals the vibronic structure of the \tilde{X}^2E_1' state of the cyclopentadienyl radical. Equation-of-motion ionization potential coupled-cluster (EOMIP-CCSD) calculations have been performed to construct a diabatic model potential of the \tilde{X}^2E_1' state, which takes into account linear Jahn–Teller effects along the e_2' normal coordinates as well as bilinear Jahn–Teller effects along the e_2' and ring-breathing a_1' coordinates. A simulation based on this *ab initio* model potential reproduces the spectrum very well, identifying the vibronic levels with linear Jahn–Teller angular momentum quantum numbers of $\pm 1/2$. The angular distributions of the photoelectrons for these vibronic levels are highly anisotropic with the photon energies used in the measurements. A few additional weak photoelectron peaks are observed when photoelectrons ejected parallel to the laser polarization are examined. These peaks correspond to the vibronic levels for out-of-plane modes in the ground \tilde{X}^2E_1'' state, which arise due to several pseudo-Jahn–Teller interactions with excited states of the radical and quadratic Jahn–Teller interaction in the \tilde{X}^2E_1' state. A variant of the first derivative of the energy for the EOMIP-CCSD method has been utilized to evaluate the strength of these nonadiabatic couplings, which have subsequently been employed to construct the model potential of the \tilde{X}^2E_1'' state with respect to the out-of-plane normal coordinates. Simulations based on the model potential successfully reproduce the weak features that become conspicuous in the 0° spectrum. The present study of the photoelectron spectrum complements a previous dispersed fluorescence spectroscopic study by Miller and co-workers [J. Chem. Phys. **114**, 4855 (2001); **114**, 4869 (2001)] to provide a detailed account of the vibronic structure of \tilde{X}^2E_1'' cyclopentadienyl. The electron affinity of the cyclopentadienyl radical is determined to be 1.808 ± 0.006 eV. This electron affinity and the gas-phase acidity of cyclopentadiene have been combined in a negative ion thermochemical cycle to determine the C–H bond dissociation energy of cyclopentadiene; $D_0(\text{C}_5\text{H}_6, \text{C–H}) = 81.5 \pm 1.3$ kcal mol⁻¹. The standard enthalpy of formation of the cyclopentadienyl radical has been determined to be $\Delta_f H_{298}(\text{C}_5\text{H}_5) = 63.2 \pm 1.4$ kcal mol⁻¹. © 2008 American Institute of Physics. [DOI: 10.1063/1.2973631]

I. INTRODUCTION

In our series of investigations of five-membered, nitrogen-containing, heterocyclic molecules, known as azoles, the influence of nitrogen atoms on thermodynamic properties, ion chemistry, and electronic structure of azoles and their derivatives has been explored.^{1–7} In particular, the photoelectron spectroscopy of the azolide ions has provided rich information on the vibronic structure of the azolyl radicals. In the case of the pyrazolyl radical,⁴ the two lowest-lying electronic states (\tilde{X}^2A_2 and \tilde{A}^2B_1) are nearly degenerate and strongly coupled by the pseudo-Jahn–Teller (PJT) effect. Furthermore, another low-lying state, \tilde{B}^2B_2 , also in-

teracts with these two states significantly. Consequently, the vibronic features observed in the photoelectron spectrum of the pyrazolide ion are manifestations of highly complicated nonadiabatic effects. In order to analyze the photoelectron spectrum, we adopted a model potential technique, developed and advocated by Köppel, Domcke, and Cederbaum (KDC).⁸ The analysis based on the KDC Hamiltonian has unveiled nonadiabatic effects in pyrazolyl.⁴

The cyclopentadienyl radical (C_5H_5) is isoelectronic with the pyrazolyl radical, but it is a more symmetric system where a C–H unit occupies each vertex of a pentagon. The D_{5h} symmetry enforces the degeneracy of the ground state of the radical (\tilde{X}^2E_1'').⁹ This state is subject to linear JT (LJT) effects¹⁰ along the e_2' normal coordinates. This nonadiabatic interaction has been a subject of numerous experimental and theoretical studies;^{11–29} C_5H_5 is a prototype JT system.

^{a)} Author to whom correspondence should be addressed.

^{b)} Electronic mail: wcl@jila.colorado.edu.

^{c)} Electronic mail: jfstanton@mail.utexas.edu.

A dispersed fluorescence study by Miller and co-workers^{26,27} is undoubtedly the most comprehensive and important work on the vibronic structure of \tilde{X}^2E_1' C₅H₅. In their study, the vibronic levels of the \tilde{X}^2E_1' state were probed through fluorescence from the \tilde{A}^2A_2'' state. Selective laser excitation to specific vibronic levels of the \tilde{A}^2A_2'' state allowed them to observe and identify not only vibronic levels of the \tilde{X}^2E_1' state which have LJT angular momentum quantum numbers (J) (Refs. 30 and 31) of $\pm 1/2$, but also those of $J = \pm 3/2$. They constructed a LJT Hamiltonian for the \tilde{X}^2E_1' state based on complete active space self-consistent field (CASSCF) calculations to carry out simulations of the fluorescence spectrum. This combination of experiment and theory provided a basic understanding of the vibronic structure of \tilde{X}^2E_1' C₅H₅.

The spectral simulation by Applegate *et al.*²⁷ is not strictly *ab initio* because while the model potential parameters were originally derived from the CASSCF calculations, they were adjusted significantly to fit the observed spectrum. In the aforementioned study of the pyrazolyl radical,⁴ we demonstrated that *ab initio* simulation can reproduce the photoelectron spectrum very well with *quadratic* model potentials parametrized by the equation-of-motion ionization potential coupled-cluster (EOMIP-CCSD) calculations.^{32,33} In the present study, we examine the vibronic structure of C₅H₅ through the photoelectron spectrum of the cyclopentadienide ion (C₅H₅⁻) utilizing a similarly parametrized model potential.

The assignment of the C₅H₅ fluorescence spectrum was complicated significantly by the appearance of several overtone and combination levels involving out-of-plane modes. Much of this complication is due to the \tilde{A}^2A_2'' state, as the presence of out-of-plane excitation in the fluorescence spectrum reflects a large difference in the potential energy surface along these coordinates between the \tilde{X}^2E_1' and \tilde{A}^2A_2'' states.³⁴ In this sense, it is desirable to isolate the JT effects in spectroscopic measurements by changing the initial state for the transition. Thus, photoelectron spectroscopy of C₅H₅⁻ offers an alternative route to explore the JT effects. The photoelectron spectrum of C₅H₅⁻ was first reported about three decades ago.¹⁸ The spectrum was quite broad due to the low resolution (60 meV) of the hemispherical kinetic energy analyzer (and, partly, due to vibrationally hot ions) and is not adequate to use as a basis for study of the vibronic structure of \tilde{X}^2E_1' C₅H₅. In the present research, we have measured the photoelectron spectrum of C₅H₅⁻ with an order of magnitude higher resolution and constructed model potentials to simulate the spectrum.

This paper is organized as follows. In Sec. II, experimental procedures for photoelectron spectroscopic measurements are described, followed by presentation of the results. Section III delineates spectral analysis using model potential techniques. Section IV contains a discussion on the vibronic structure of \tilde{X}^2E_1' C₅H₅ and a comparison with the previous dispersed fluorescence study. The thermochemistry of the radical is also discussed. Section V concludes.

II. PHOTOELECTRON SPECTROSCOPY

A. Experimental procedure

The negative ion photoelectron spectroscopic apparatus has been described in detail elsewhere.^{35–37} The ions are synthesized in a flowing afterglow ion source. A microwave discharge of helium buffer gas (~ 0.4 Torr) with a trace amount of oxygen generates the atomic oxygen radical anion (O⁻). Methane (CH₄) is introduced downstream and reacts with O⁻ to convert it to the hydroxide ion (HO⁻). Cyclopentadiene (C₅H₆) is introduced further downstream and reacts with HO⁻ to produce C₅H₅⁻. The liquid sample of C₅H₆ is freshly prepared by fractional distillation of the dimer (dicyclopentadiene, Aldrich). The C₅H₅⁻ ions are thermalized through collisions with the buffer gas in a flow tube which is cooled by liquid nitrogen. This procedure typically achieves an ion temperature of ≈ 200 K. The ions are extracted into a differentially pumped region, accelerated to 740 eV, and focused into a Wien velocity filter for mass selection. The mass-selected ions are refocused and decelerated to 35 eV, and this C₅H₅⁻ ion beam (typically ~ 100 pA) is crossed with an intense photodetachment laser beam. Approximately 1 W of either 351.1 or 363.8 nm (3.531 or 3.408 eV) single-frequency argon ion laser emission is injected into a high-vacuum build-up cavity for photodetachment. The circulating power is ~ 100 W, where the ion and laser beams overlap.

Photoelectrons emitted in a small solid angle perpendicular to both the ion and laser beams are focused into a hemispherical energy analyzer. The energy-analyzed electrons are accelerated and magnified onto microchannel plates for amplification and imaged onto a position-sensitive detector. The kinetic energy resolution of the analyzer system is 8–10 meV (65–80 cm⁻¹). Photoelectron spectra are constructed as a function of electron binding energy (eBE), which is the laser photon energy minus the electron kinetic energy (eKE). The absolute energy of the electrons is calibrated through the measurement of a photoelectron spectrum of O⁻ with the very accurately known electron affinity (EA) of the oxygen atom.³⁸ The energy scale is also corrected for a small linear energy compression factor ($< 1\%$),³⁵ which is determined from the measurements of photoelectron spectra of O⁻, S⁻, and I⁻ utilizing the EAs of the corresponding atoms.³⁹ A rotatable half-wave plate controls the direction of the laser polarization, and the angular distribution of the photoelectrons is given by⁴⁰

$$I(\theta) = \frac{\sigma_0}{4\pi} (1 + \beta P_2(\cos \theta)), \quad (1)$$

where θ is the angle between the laser polarization and the photoelectron momentum vectors, and σ_0 and β are the total photodetachment cross section and the anisotropy parameter, respectively, at the corresponding photoelectron kinetic energy. Also, $P_2(\cos \theta) = (3 \cos^2 \theta - 1)/2$ is the second Legendre polynomial. The β dependence of the photoelectron counts vanishes in the measurements at the magic angle ($\theta = 54.7^\circ$), providing a spectrum where photoelectron intensities are uniformly proportional to σ_0 at all kinetic energies.

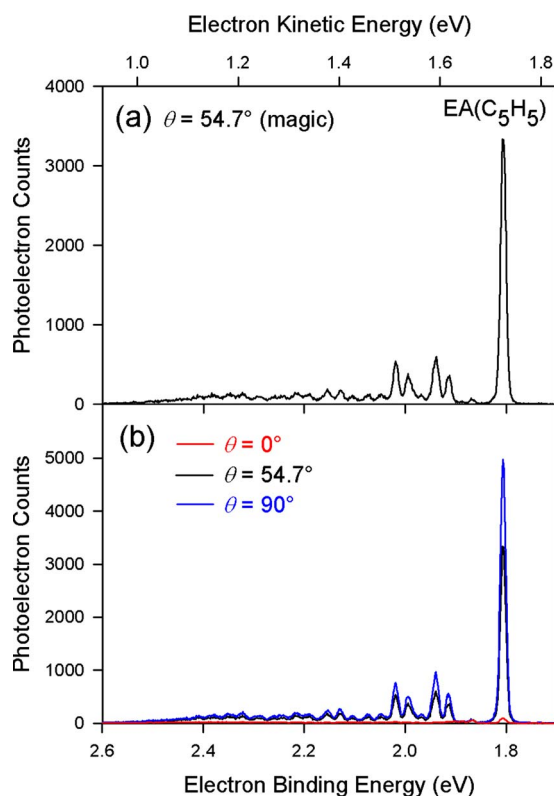


FIG. 1. (Color online) The 351.1 nm photoelectron spectra of the cyclopentadienide ion. (a) A spectrum taken at the magic angle. (b) Spectra taken at $\theta=54.7^\circ$ (black), 0° (red), and 90° (blue).

The β values are determined by measuring the photoelectron detachment rates for $\theta=0^\circ$, 54.7° , and 90° .

B. Results

Figure 1(a) shows the 351.1 nm photoelectron spectrum of $C_5H_5^-$ taken at the magic angle. An intense peak appears at eBE of ~ 1.8 eV. In light of the assignments established for isoelectronic azolyl radicals,¹⁻⁴ this peak clearly arises from the transition from the ground level of $C_5H_5^-$ to that of C_5H_5 . Indeed, our spectral simulation, detailed in a later section, confirms this assignment. The EA of C_5H_5 is thus 1.808 ± 0.006 eV. To the higher eBE side of the spectrum, a few peaks of moderate intensity are observed together with a number of peaks and bands of smaller intensity. Figure 1(b) shows the photoelectron spectra of $C_5H_5^-$ taken at different θ values [see Eq. (1)]. When θ is 90° , the spectral profile is very similar to that of the magic angle spectrum but the intensities are larger ($\beta < 0$). On the other hand, the overall photoelectron intensities diminish drastically when θ is 0° .

In fact, the 0° spectrum bears a profile that is quite distinct from the magic angle or 90° spectrum. The magic angle and 0° spectra are compared more clearly in Fig. 2. Note the different scales of photoelectron counts for Figs. 2(a) and 2(b). While the intensity of peak *b* relative to that of the origin peak (peak *a*) is very small in the magic angle spectrum [see also Fig. 1(a)], it is relatively much more intense in the 0° spectrum. The same statement applies to peak *c*, and peaks *d*, *h*, and *j* are not even noticeable in the magic angle spectrum (see discussion below).

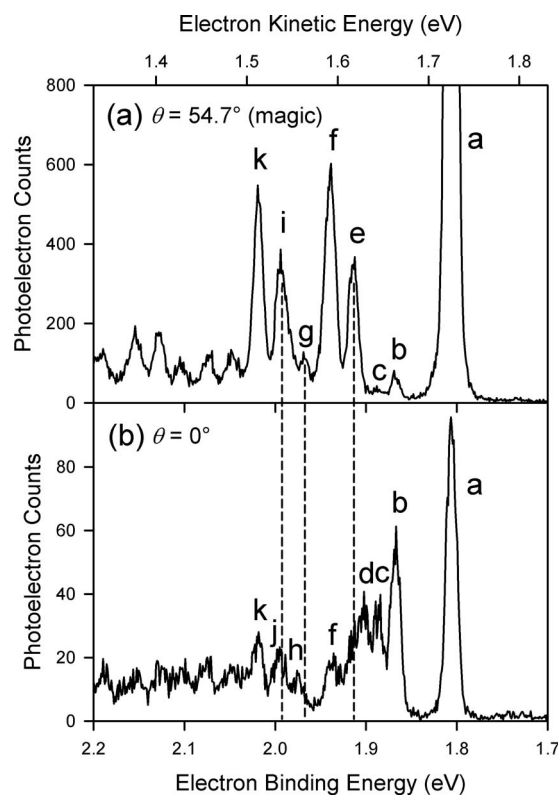


FIG. 2. The 351.1 nm photoelectron spectra of the cyclopentadienide ion taken at (a) $\theta=54.7^\circ$ and (b) $\theta=0^\circ$. Note the different scales of photoelectron counts.

Angular distributions of photoelectrons are characterized by the anisotropy parameter, β [Eq. (1)]. We have determined the β values for peaks *a* and *b* to be -0.972 ± 0.004 and -0.15 ± 0.15 , respectively, at 351.1 nm. The photoelectrons for peaks *b*, *c*, *d*, *h*, and *j* have much less negative β values (are much more isotropic) than those for the peaks prominent in the magic angle spectrum (peaks *a*, *e*, *f*, *g*, *i*, and *k*). Evidently, the cross sections for photodetachment for these latter (major) peaks are much larger than those for peaks *b*, *c*, *d*, *h*, and *j*. It is the highly anisotropic nature of the photoelectrons for the major peaks that allows observation of those minor peaks at $\theta=0^\circ$.^{41,42} These effects of anisotropic photoelectrons on the spectral profile can also be appreciated when the 351.1 nm spectra are compared with the spectra taken with 363.8 nm laser beam, as described in the EPAPS document.⁴³

Table I summarizes the peak positions observed in the photoelectron spectra. In Sec. III, the analysis of the spectra is carried out based on a model potential technique.

III. SPECTRAL ANALYSIS

A model potential technique, developed and advocated by KDC,⁸ has been adopted to analyze the photoelectron spectra of $C_5H_5^-$ in the present study. Details of the technique have been well documented in the literature,^{4,8,44} which should be consulted for further information.

TABLE I. Peak positions (cm^{-1}) and assignments for the photoelectron spectrum of the cyclopentadienide ion. See Fig. 2 for peak labels.

Peak	Position	Assignment	Vibronic (vibrational) symmetry
<i>a</i>	0	Ground level	e_1''
<i>b</i>	500 ± 7	ν_{14}^1	$e_1' + e_2' (e_2'')$
<i>c</i>	657 ± 20	ν_4^1	$e_1' (a_2')$
<i>d</i>	778 ± 20	ν_8^1	$e_2' (e_1')$
<i>e</i>	875 ± 12	$J = \pm 1/2, 1$	$e_1'' (e_2')$
<i>f</i>	1078 ± 10	$J = \pm 1/2, 2$	$e_1'' (a_1', e_2')$
<i>g</i>	1313 ± 21	$J = \pm 1/2, 4$	$e_1'' (a_1', e_2')$
<i>h</i>	1379 ± 17	ν_8^2	$e_1'' (a_1', e_2')$
<i>i</i>	1512 ± 14	$J = \pm 1/2, 5$	$e_1'' (a_1', e_2')$
<i>j</i>	1533 ± 15	ν_8^2	$e_1'' (a_1', e_2')$
<i>k</i>	1716 ± 15	$J = \pm 1/2, 6+7$	$e_1'' (a_1', e_2')$

A. LJT effects

According to its vibronic symmetry, $\tilde{X}^2E_1'' C_5H_5^-$ is LJT active along the e_2' normal coordinates. [Table II displays the direct products of irreducible representations of the D_5 point group for reference. This table, in conjunction with the usual rules governing direct products of representations that are symmetric (') and antisymmetric (") with respect to reflections in a plane, suffices to facilitate understanding of the group theoretical arguments in this paper.] The model potential needs to incorporate the LJT couplings in order to predict their effects in spectral simulation. Analogous to our previous study on the isoelectronic pyrazolyl system,⁴ the normal coordinates of the initial state for the photodetachment process, i.e., the electronic ground state of $C_5H_5^-$, are used to construct the model potential.

The equilibrium geometry of $\tilde{X}^1A_1' C_5H_5^-$ has been determined with coupled-cluster singles and doubles (CCSD) calculations⁴⁵ using the Huzinaga–Dunning double-zeta plus polarization (DZP) basis set.^{46,47} The *ab initio* calculations have been performed with the ACES II program package.⁴⁸ The C–C and C–H equilibrium bond lengths have been calculated to be 1.4254 and 1.0938 Å, respectively. Quadratic force constants have been calculated using analytic second derivatives,⁴⁹ and the information on the normal modes is given in Table III. There are four LJT-active e_2' modes in $\tilde{X}^2E_1'' C_5H_5^-$. These four degenerate vibrations can be resolved such that one component preserves the C_{2v} Abelian subgroup symmetry, while the other lowers it to C_s . Figure 3 shows the atomic displacements of the symmetric components of these degenerate modes as well as diagrams for out-of-plane modes.

Parametrization of model potentials has been discussed

TABLE II. Direct products of irreducible representations of the D_5 point group.

	a_1	a_2	e_1	e_2
a_1	a_1	a_2	e_1	e_2
a_2		a_1	e_1	e_2
e_1			$a_1 + a_2 + e_2$	$e_1 + e_2$
e_2				$a_1 + a_2 + e_1$

TABLE III. Harmonic vibrational frequencies (cm^{-1}) of the \tilde{X}^1A_1' state of the cyclopentadienide ion evaluated with CCSD/DZP calculations.

$\tilde{X}^1A_1' C_5H_5^-$					
Mode	Symmetry	Frequency	Mode	Symmetry	Frequency
1	a_1'	3221	8	e_1''	528
2		1157	9	e_2'	3169
3	a_2'	1267	10		1434
4	a_2''	618	11		1063
5	e_1'	3196	12		834
6		1488	13	e_2''	709
7		1021	14		604

extensively.^{4,8,26,44,50} Basically, there are two types of parametrization for linear coupling constants. One is to take the derivative of the energy at the reference geometry, i.e., the equilibrium geometry of $\tilde{X}^1A_1' C_5H_5^-$, which has been termed “vertical κ ” previously.⁴ The other is “adiabatic κ ,” which is a product of the displacements of the equilibrium geometries from the initial to final states of the transition and the quadratic force constant matrix of the final state at its equilibrium geometry.⁴

Energy gradients have been calculated analytically at the anion geometry for $\tilde{X}^2E_1'' C_5H_5^-$ (i.e., 2A_2 and 2B_1 symmetries in the C_{2v} Abelian subgroup) with the EOMIP-CCSD method,³² and they are shown in Table IV. The vertical κ 's for the e_2' modes represent the nominal strength of the LJT couplings. The table also gives gradients with respect to the two a_1' modes; one is the ring-breathing mode (ν_2) and the other is the C–H stretching mode (ν_1). In order to evaluate adiabatic κ 's, the equilibrium geometries of the 2A_2 and 2B_1 states have been located with EOMIP-CCSD/DZP calculations, and the geometry parameters are given as displace-

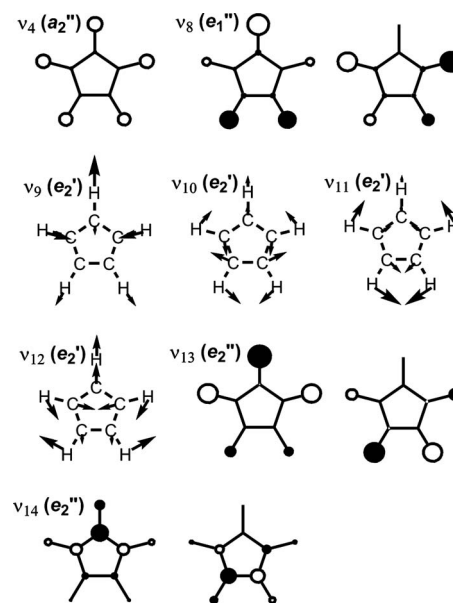


FIG. 3. Relative atomic displacements for the normal modes of the \tilde{X}^1A_1' state of the cyclopentadienide ion evaluated with CCSD/DZP calculations. For the out-of-plane modes, the diameters of the circles represent the relative magnitudes of displacements, while open and filled circles represent the opposite phases of displacements.

TABLE IV. Linear coupling constants (eV) for the \tilde{X}^2E_1' state of the cyclopentadienyl radical evaluated with EOMIP-CCSD/DZP calculations.

Mode	Symmetry	\tilde{X}^2E_1' C ₅ H ₅			
		Vertical κ		Adiabatic κ	
		² A ₂	² B ₁	² A ₂	² B ₁
1	<i>a</i> ' ₁	-0.0504	-0.0504	-0.0455	-0.0455
2		0.0036	0.0036	-0.0234	-0.0234
9	<i>e</i> ' ₂	0.0055	-0.0055	0.0054	-0.0054
10		0.2128	-0.2128	0.2128	-0.2123
11		-0.1144	0.1144	-0.1150	0.1148
12		-0.0638	0.0638	-0.0625	0.0626

ments from the equilibrium geometry of \tilde{X}^1A_1' C₅H₅⁻ in Table V. The bond lengths and angles are provided in the EPAPS document.⁴³ Quadratic force constants have been calculated for the ²A₂ and ²B₁ states at the corresponding optimized geometries using finite differences of analytic first derivatives.³² The resultant harmonic frequencies are also given in the EPAPS document.⁴³ The calculations find the ²B₁ state to be a minimum and the ²A₂ state to be a transition state, with an imaginary frequency of just 46i cm⁻¹ for a *b*₂ mode in the latter. The potential energy difference between the minimum and the transition state is only 0.045 meV. This is, of course, to be expected in this case, as quadratic JT (QJT) activity¹⁰ is impossible along the *e*'₂ coordinates in the \tilde{X}^2E_1' state, and any pseudorotation barrier necessarily arises from different high-order coupling mechanisms (see below). Adiabatic κ 's are evaluated from the geometry displacements and the quadratic force constants, and they are given in Table IV along with the vertical κ 's.

In our previous study on the photoelectron spectra of the pyrazolide and imidazolide ions, we have discussed how the anharmonicity of the potential energy surfaces and Duschinsky rotation affects parametrization of the model potential.⁴ Significant differences were found between the vertical and adiabatic κ 's for the low-lying states of the pyrazolyl and imidazolyl radicals, and considerable effects of the anharmonicity in the spectral simulation have been noted.⁴ In con-

TABLE V. Equilibrium geometries of the \tilde{X}^2E_1' state of the cyclopentadienyl radical located with EOMIP-CCSD/DZP calculations. Geometries are expressed as displacements from the equilibrium geometry of \tilde{X}^1A_1' cyclopentadienide ion in terms of the anion reduced normal coordinates.

Mode	Symmetry	\tilde{X}^2E_1' C ₅ H ₅	
		² A ₂	² B ₁
1	<i>a</i> ' ₁	0.1266	0.1266
2		-0.1212	-0.1214
5	<i>e</i> ' ₁	-0.0048	-0.0037
6		-0.0305	-0.0251
7		0.0477	0.0403
9	<i>e</i> ' ₂	-0.0134	0.0133
10		-1.1207	1.1211
11		0.8286	-0.8289
12		0.6642	-0.6638

trast, the linear vertical and adiabatic κ 's are very similar to each other for \tilde{X}^2E_1' C₅H₅ (Table IV). The κ 's for the ²A₂ and ²B₁ states for each *e*'₂ mode have an equal magnitude with opposite signs, which is a consequence of the *D*_{5h} symmetry of the expansion point. The magnitudes of the adiabatic κ 's are only slightly different between the ²A₂ and ²B₁ states, indicative of small higher-order effects. The absence of significant anharmonic effects in the corresponding portion of the potential energy surfaces of \tilde{X}^2E_1' C₅H₅ can be corroborated by the data provided so far. The equilibrium geometries in Table V show that the displacements along the *e*'₂ normal coordinates for the ²A₂ and ²B₁ states are very similar in magnitude and opposite in phase. In a pure LJT system, the magnitude of the displacements should be identical for the two states with opposite phases. Also, a pure LJT system has no energy variation along its pseudorotation path. The very small energy difference between the ²B₁ minimum and ²A₂ transition state mentioned above also reflects very small higher-order and/or PJT couplings and intrinsic anharmonicity. These effects also lead to small displacements along the (LJT-inactive) *e*'₁ normal coordinates for the equilibrium geometries of the ²A₂ and ²B₁ states shown in Table V.

As for the *a*'₁ modes, both the magnitude and sign of the linear coupling constants are the same for the ²A₂ and ²B₁ states because displacement along the *a*'₁ normal coordinates does not lift the degeneracy of the \tilde{X}^2E_1' state. While the vertical and adiabatic κ 's are only slightly different for ν_1 , there is a significant difference between the vertical and adiabatic κ 's for ν_2 mode (Table IV). This observation is directly related to the important mode mixing effects, as will be discussed later.

At this point, we construct the LJT model potential for \tilde{X}^2E_1' C₅H₅. Because of the similarity, whether the vertical κ 's or adiabatic κ 's are employed in the model potential has no important consequences in the spectral simulation. Considering the successful results attained for the pyrazolyl and imidazolyl radicals in our previous study,⁴ the adiabatic κ 's are adopted. The magnitudes of the adiabatic κ 's for the ²A₂ and ²B₁ states shown in Table IV are averaged to construct a pure LJT model Hamiltonian,

$$H = (T_N + V_0 + E_X)I + V,$$

$$T_N = -\frac{1}{2} \sum_i \omega_i \frac{\partial^2}{\partial q_i^2},$$

$$V_0 = \frac{1}{2} \sum_i \omega_i q_i^2,$$

$$V = \begin{pmatrix} \kappa_2 q_2 + \sum_{i \in e'_2} \kappa_i q_{i,x} & \sum_{i \in e'_2} \kappa_i q_{i,y} \\ \sum_{i \in e'_2} \kappa_i q_{i,y} & \kappa_2 q_2 - \sum_{i \in e'_2} \kappa_i q_{i,x} \end{pmatrix}. \quad (2)$$

Here, T_N is the nuclear kinetic energy operator, V_0 is the potential energy of the reference state, i.e., \tilde{X}^1A_1' C₅H₅⁻, E_X is the vertical detachment energy for the \tilde{X}^2E_1' state, and I is the identity matrix. Also, ω_i and q_i are the harmonic vibra-

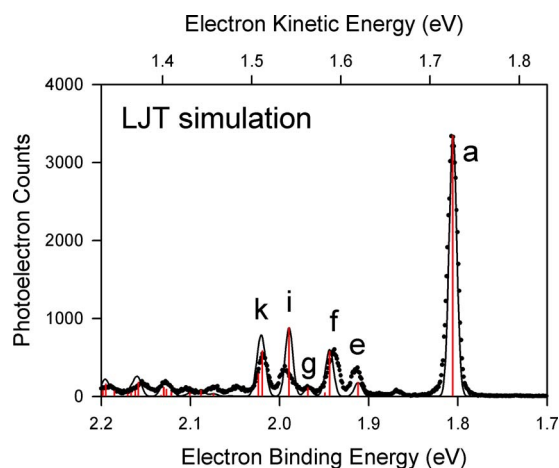


FIG. 4. (Color online) A simulation for the \tilde{X}^2E_1' state of the cyclopentadienyl radical based on the model potential of Eq. (2) accounting for LJT effects. The sticks (red) represent the positions and relative intensities of individual transitions to vibronic levels of e_1' symmetry. The solid line is the simulated spectrum with a Gaussian convolution of a 10 meV full width at half maximum, superimposed on the experimental spectrum (dots).

tional frequencies and the reduced normal coordinates of the reference state. It is important to note that $q_{i,x}$ is the symmetric component (with respect to C_{2v}) of the degenerate mode, and $q_{i,y}$ is the other component orthogonal to the former (b_2 in C_{2v}). The linear coupling constants κ_i are as parametrized above (Table IV). Among the a_1' and e_2' modes, the C–H stretching high frequency modes (ν_1 and ν_9) are excluded from the model potential because they do not make significant contributions to spectral simulation.

Spectral simulations have been performed as previously described.^{4,44,51} Figure 4 shows the result of the simulation based on the model potential of Eq. (2),⁵² superimposed on the observed magic angle photoelectron spectrum of $C_5H_5^-$.

The simulation predicts an intense origin peak, which agrees with the observed spectrum. Also, the simulation reproduces the positions of peaks *e*, *f*, *g*, *i*, and *k* very well. Thus, the simulation is consistent with the assignment of these peaks as vibronic levels of $J = \pm 1/2$. The small linear coupling constant for the a_1' mode (ν_2 , see Table IV) results in a negligible contribution to the spectral simulation based on the model potential of Eq. (2) (see also discussion below).

B. Bilinear JT effects

While the positions of prominent peaks observed in the magic angle spectrum are well predicted by the LJT model Hamiltonian, the relative intensities of those peaks are not so well reproduced by the simulation. For instance, besides the origin peak, the most intense peak is peak *f* in the observed magic angle spectrum, but the simulation predicts peak *i* to be the most intense (Fig. 4). It is well known that the spectral intensity is often significantly affected by Duschinsky mode mixing, which is not present in the LJT treatment.⁵³ In this section, possible quadratic effects in the spectral simulation are examined.

Following the arguments made in our previous study,⁴ quadratic parametrization of the model potential utilizes force constants calculated at the corresponding equilibrium geometries of the 2A_2 and 2B_1 states of C_5H_5 (i.e., adiabatic κ). The quadratic coupling constants obtained with EOMIP-CCSD/DZP calculations are listed in Table VI.

Similarity of the quadratic coupling constants within the a_1' block and e_2' block between the two states is obvious in Table VI. None of these quadratic couplings is large, and the magnitudes of the mode mixing within the diagonal blocks are very small. On the other hand, the quadratic couplings between the a_1' mode and the e_2' mode for the 2A_2 and 2B_1 states have the same magnitude and opposite signs, as they

TABLE VI. Quadratic coupling constants (eV) for the \tilde{X}^2E_1' state of the cyclopentadienyl radical evaluated with EOMIP-CCSD/DZP calculations.

		$\tilde{X}^2E_1' C_5H_5, ^2A_2$					
Mode		1	2	9	10	11	12
	Symmetry	a_1'		e_2'			
1	a_1'	0.0185	-0.0014	-0.0025	0.0084	0.0043	-0.0026
2			0.0001	0.0016	-0.0281	0.0116	-0.0001
9	e_2'			0.0233	-0.0044	-0.0012	-0.0050
10					0.0164	-0.0029	0.0025
11						0.0085	-0.0048
12							0.0015
		$\tilde{X}^2E_1' C_5H_5, ^2B_1$					
Mode		1	2	9	10	11	12
	Symmetry	a_1'		e_2'			
1	a_1'	0.0185	-0.0014	0.0025	-0.0084	-0.0043	0.0026
2			0.0001	-0.0016	0.0281	-0.0116	0.0001
9	e_2'			0.0233	-0.0043	-0.0012	-0.0050
10					0.0157	-0.0026	0.0024
11						0.0084	-0.0048
12							0.0014

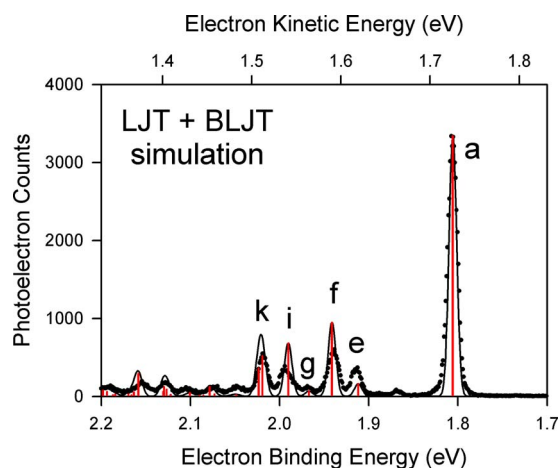


FIG. 5. (Color online) A simulation for the \tilde{X}^2E_1' state of the cyclopentadienyl radical, based on the model potential of Eqs. (2) and (3) accounting for LJT and BLJT effects. The sticks (red) represent the positions and relative intensities of individual transitions to vibronic levels of e_1'' symmetry. The solid line is the simulated spectrum with a Gaussian convolution of a 10 meV full width at half maximum, superimposed on the experimental spectrum (dots).

must. The largest among these quadratic couplings is that between ν_2 and ν_{10} . This relatively large coupling may be understandable when the normal coordinates are compared. The ν_{10} mode involves mainly C–C stretching motion (Fig. 3), while the ν_2 mode is totally symmetric C–C stretching. In contrast, the ν_{12} mode represents CCC bending motion without C–C stretching, and there is virtually no quadratic mixing between ν_2 and ν_{12} . The quadratic coupling of the a_1' mode and the e_2' mode is often termed as bilinear coupling.⁵⁴ Overall, the bilinear couplings involving the ν_2 mode are much larger than those involving the ν_1 mode. The bilinear couplings are also responsible for the significant difference in linear coupling between the vertical and adiabatic κ 's for the ν_2 mode (Table IV).⁵⁵

Now, we supplement the model potential of Eq. (2) with the following bilinear Jahn–Teller (BLJT) terms:

$$V = \begin{pmatrix} \sum_{j \in e_2'} \kappa_{2,j} q_{2j,x} & \sum_{j \in e_2'} \kappa_{2,j} q_{2j,y} \\ \sum_{j \in e_2'} \kappa_{2,j} q_{2j,y} & -\sum_{j \in e_2'} \kappa_{2,j} q_{2j,x} \end{pmatrix}. \quad (3)$$

As in the construction of linear model potential, ν_1 and ν_9 modes are excluded. The small mixing terms involving these two modes (Table VI) justify this approximation.

Figure 5 shows the result of the simulation based on the model potential including the BLJT effects in Eq. (3). Comparison with the simulation based on linear model potential (Fig. 4) shows the effects of the quadratic terms of the model potential. While the *positions* of major peaks change only marginally, the BLJT terms alter the relative *intensities* of the peaks significantly. It is particularly noteworthy that, after inclusion of the bilinear couplings, the predicted relative intensities match the experimental profile quite well.

C. PJT and QJT effects

A BLJT model [Eqs. (2) and (3)] quite satisfactorily reproduces the prominent features of the observed magic angle

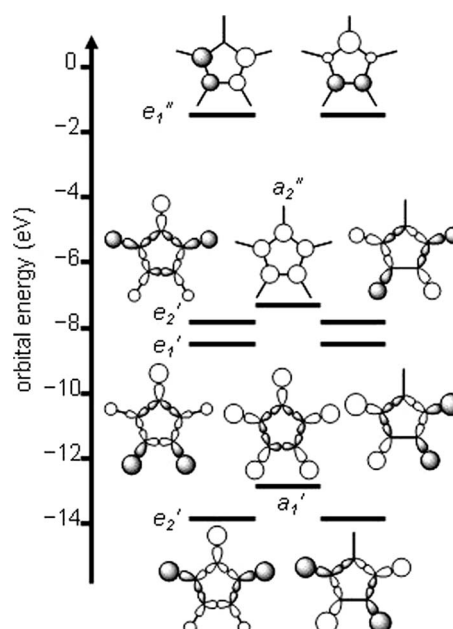


FIG. 6. Schematic representations of the highest occupied molecular orbitals of the \tilde{X}^1A_1' state of the cyclopentadienide ion and their energy diagram obtained from SCF calculations.

photoelectron spectrum of $C_5H_5^-$ but gives no account of the features between 500 and 800 cm^{-1} (with respect to the origin) which are more noticeable in the 0° spectrum [Fig. 2(b)]. In the photoelectron spectrum for another JT system, the methoxy radical (CH_3O),^{56–59} the appearance of weak $J = \pm 3/2$ peaks, which have β values quite distinct from those for intense $J = \pm 1/2$ peaks, is most likely due to a PJT interaction between \tilde{X}^2E and \tilde{A}^2A_1 CH_3O .^{60,61} It is plausible, therefore, to investigate related PJT effects that are operative in C_5H_5 . A difference exists with CH_3O , however, as the LJT-active e_2' modes cannot have appreciable PJT activity for \tilde{X}^2E_1'' C_5H_5 owing to the absence of proximal excited states having appropriate E_1' or E_2'' symmetry (see also Ref. 62). Consequently, the aforementioned weak peaks in the 0° spectrum are almost certainly not $J = \pm 3/2$ features of \tilde{X}^2E_1'' C_5H_5 .

Figure 6 schematically illustrates the highest occupied molecular orbitals of \tilde{X}^1A_1' $C_5H_5^-$ obtained from SCF calculations. The removal of a single electron from each of these orbitals in the reference determinant results in a dominant electronic configuration for a unique electronic state of C_5H_5 that is accessible in single-photon detachment events. Figure 7 displays an EOMIP-CCSD/DZP energy diagram for the electronic states of C_5H_5 at the equilibrium geometry of \tilde{X}^1A_1' C_5H_5 .⁶² The \tilde{A}^2A_2'' state has been a subject of previous experimental studies, but, to the best of our knowledge, none of the higher excited states has been studied, experimentally or theoretically.

In model potential techniques, the linear interstate coupling constant for mode i ($\lambda_{i,A,B}$) is usually evaluated from the quadratic force constants of the two relevant adiabatic states ($f_{i,A}$ and $f_{i,B}$) as follows:⁶³

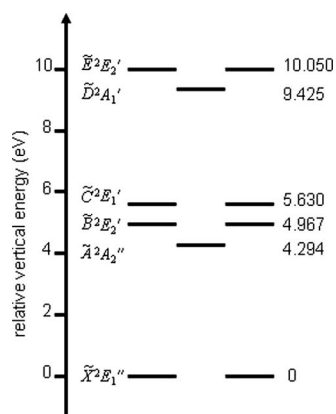


FIG. 7. Relative vertical energies of the electronic states of the cyclopentadienyl radical evaluated with EOMIP-CCSD/DZP calculations.

$$|\lambda_{i,A,B}| = \frac{1}{2} \sqrt{\Delta E (f_{i,A} - f_{i,B})}. \quad (4)$$

Here, ΔE is the vertical energy separation of the two adiabatic states. This simple formula rests on two fundamental assumptions. The first is that the diabatic force constants in the two coupled states are the same, and the second is that these two states are vibronically isolated from the remainder of states. In many cases, these are quite good assumptions (the BNB radical⁶⁴ is a prime example) but Eq. (4) cannot be applied with confidence in many situations. In C_5H_5 , for example, PJT coupling along the e_1'' mode mixes the \tilde{X}^2E_1'' state with the \tilde{B}^2E_2' , \tilde{D}^2A_1' , and \tilde{E}^2E_2' states, and a two-state model is clearly not applicable.

However, Gauss and Stanton have recently worked out a formalism for the direct analytic calculation of λ constants, subject to a suitable definition of diabatic states, which are taken to be based on the description of the nearby closed-shell anion, within the EOMIP-CCSD method. Details will be published in the future,⁶⁵ but suffice it to say that λ parameters calculated with Eq. (4) and analytically with EOMIP-CCSD agree to much better than 1% in a favorable model system such as the BNB radical. As a further numerical check, the λ constants for the LJT couplings in \tilde{X}^2E_1'' C_5H_5 have been evaluated analytically [along the asymmetric components of the e_2'' modes; these λ constants are denoted as κ in the off-diagonal elements of the potential matrix in Eq. (2)]. The resultant values are identical with those given in Table IV (i.e., vertical κ), which are based on the

analytic first derivative of energy as the linear intrastate coupling.⁶⁶ Other numerical checks are given in EPAPS.⁴³

Linear interstate coupling constants for the vibronic interaction of the \tilde{X}^2E_1'' state with the excited states shown in Fig. 7 have been calculated analytically, and these “analytic λ ” constants are listed in Table VII. Considerable PJT interactions have been found that mix the ground with all the excited states considered in this work. Therefore, the truncated vibronic basis for the model Hamiltonian should take all these electronic states into account. Simultaneous inclusion of all the electronic states and all the vibrational modes in the model Hamiltonian, however, is computationally cumbersome, and also necessitates parametrization for all the excited states. Instead, we adopt a simplified approach to the problem at hand (i.e., spectral analysis for the \tilde{X}^2E_1'' state). Model potentials are constructed in terms of normal modes of a particular symmetry at a time, independently of those of the other symmetries. Moreover, only couplings directly involving the \tilde{X}^2E_1'' state are considered in constructing the model potentials. Details of these quadratic Hamiltonians are given in the EPAPS document,⁴³ while Table VIII displays the coupling constants that have been used.

Simulations based on the model potentials have been performed, and the results are shown in Fig. 8. In these plots, the intensity of the origin peak is set to unity; the intensity scale is chosen to focus on weak peaks predicted by the simulations.

1. a_2'' mode coupling

Figure 8(a) shows the spectrum simulated with the model potential along the a_2'' mode. Besides the intense origin peak, the simulation predicts two weak peaks. One is a peak for a vibronic level of e_1' symmetry and the other is that of e_1'' symmetry (i.e., the same symmetry as that of the origin peak). Clearly, the intensity of the fundamental peak for the a_2'' mode originates from the transition dipole moment for the detachment to the \tilde{C}^2E_1' state. In other words, the appearance of the peak in the simulation is attributed to PJT interaction between the \tilde{X}^2E_1'' and \tilde{C}^2E_1' states. On the other hand, the intensity of the overtone peak stems from the quadratic intrastate coupling as well as the linear interstate coupling.

TABLE VII. Linear interstate coupling constants (eV) for the \tilde{X}^2E_1'' state of the cyclopentadienyl radical evaluated with EOMIP-CCSD/DZP calculations.

Mode	Symmetry	Analytic λ , C_5H_5 , $\tilde{X}^2E_1'' \leftrightarrow$				
		\tilde{A}^2A_2''	\tilde{B}^2E_2'	\tilde{C}^2E_1'	\tilde{D}^2A_1'	\tilde{E}^2E_2'
4	a_2''			0.3645		
5	e_1'	0.0229				
6		-0.1838				
7		-0.1107				
8	e_1''		-0.2228		-0.2973	0.2202
13	e_2''		-0.1497	0.2044		0.2300
14			-0.1478	0.0838		-0.0510

TABLE VIII. Quadratic coupling constants (eV) for the \tilde{X}^2E_1'' state of the cyclopentadienyl radical evaluated with EOMIP-CCSD/DZP calculations.

Mode	$\kappa_{i,j}, \tilde{X}^2E_1'' C_5H_5$							
		4	5	6	7	8	13	14
Symmetry		a_2''	e_1'			e_1''	e_2''	
4	a_2''	0.0674						
5	e_1'		0.0086	0.0012	-0.0027			
6				0.0081	-0.0020			
7					0.0092			
8	e_1''					0.1022		
13	e_2''						0.0624	-0.0200
14								0.0114
$\tilde{X}^2E_1'' C_5H_5$								
Mode		5		6		7		8
Symmetry		e_1'						e_1''
$\kappa_{i,i,QJT}$		0.0005		0.0086		0.0043		0.0302

2. e_1' mode coupling

Compared to the peaks for the a_2'' mode, those for the e_1' modes have even smaller predicted intensities based on the corresponding model potential, as shown in Fig. 8(b). Even though the energy separation between the \tilde{X}^2E_1'' and \tilde{A}^2A_2'' states is smaller than that between the \tilde{X}^2E_1'' and \tilde{C}^2E_1' states (see Fig. 7), the interstate coupling constants for the e_1' modes are much smaller than that for the a_2'' mode (Table VII). As a result, the corresponding fundamental peaks cannot gain their intensity as much through the nonadiabatic effects. The quadratic coupling constants for the e_1' modes are also much smaller than that for the a_2'' mode (Table VIII), explaining the very weak overtone peaks in Fig. 8(b).

3. e_1'' mode coupling

In the simulation that includes e_1'' mode coupling, shown in Fig. 8(c), one peak for a vibronic level of e_2' symmetry (~ 90 meV above the origin peak) and two peaks for those of e_1'' symmetry (~ 160 and ~ 200 meV) are easily noticeable besides the origin peak. The peak of e_2' symmetry, which represents the fundamental level of the e_1'' mode, appears due to the PJT interaction of the \tilde{X}^2E_1'' state with two excited states: \tilde{B}^2E_2' and \tilde{E}^2E_2' states.⁶⁷ On the other hand, the PJT interaction with the \tilde{D}^2A_1' state provides the other fundamental peak (i.e., a_1' vibronic symmetry) with only very small intensity, as shown in Fig. 8(c).

The peaks of e_1'' symmetry represent two separate overtone levels associated with the e_1'' mode. The splitting of the overtone level (which we will discuss later) arises from the QJT interaction¹⁰ in the \tilde{X}^2E_1'' state and the PJT interaction of the \tilde{X}^2E_1'' state with the \tilde{D}^2A_1' state. The intensity of the overtone peaks originates from the quadratic intrastate coupling, the QJT coupling, and the PJT coupling for the e_1'' mode (Tables VII and VIII).

4. e_2'' mode coupling

The simulation including the e_2'' mode coupling predicts two peaks for the fundamental levels of ν_{13} (~ 110 meV above the origin peak) and ν_{14} (~ 70 meV), as shown in Fig. 8(d). Each peak has two components. One has e_2' vibronic symmetry and arises from the PJT interactions with the \tilde{B}^2E_2' and \tilde{E}^2E_2' states. The PJT interaction with the \tilde{C}^2E_1' state gives rise to the other sublevel which has e_1' vibronic symmetry. The simulation also displays the overtone peaks for the two e_2'' modes as well as their combination peak. The source of their intensities is the PJT interaction as well as the quadratic intrastate coupling.

5. Assignments of the 0° spectrum

We now attempt to analyze weaker features in the 0° spectrum, shown in Fig. 2(b), based on the simulations shown in Fig. 8. As described in Secs. III A and III B, peaks b , c , d , h , and j are not associated with the LJT coupling along the e_2' coordinates. Among these peaks, peaks b , c , and d are located in the spectrum such that they appear to correspond to the fundamental levels of the out-of-plane modes. Judging from the peak positions in the simulated spectra in Fig. 8, peaks b , c , and d most probably represent the fundamental levels of an e_2'' (ν_{14}), a_2'' (ν_4), and e_1'' (ν_8) modes, respectively. The intensities of these peaks relative to the origin peak in the simulated spectra are also broadly consistent with the observed spectrum.^{68,69}

Relatively simple considerations further demonstrate that these assignments are lent plausibility by the angular distributions of the photoelectrons observed in the experiment. For states of e_1'' vibronic symmetry, group theoretical considerations⁷⁰ suggest that the dominant transition moment component for photodetachment lies along the C_5 symmetry axis (a_2''), with an outgoing electron that is principally of p wave character (e_1'). This situation leads to the prediction of small intensities in the 0° spectrum. Conversely, detachment to e_1' or e_2' vibronic level of C_5H_5 with x or y polarized radiation (e_1') is accompanied by electrons of either s wave

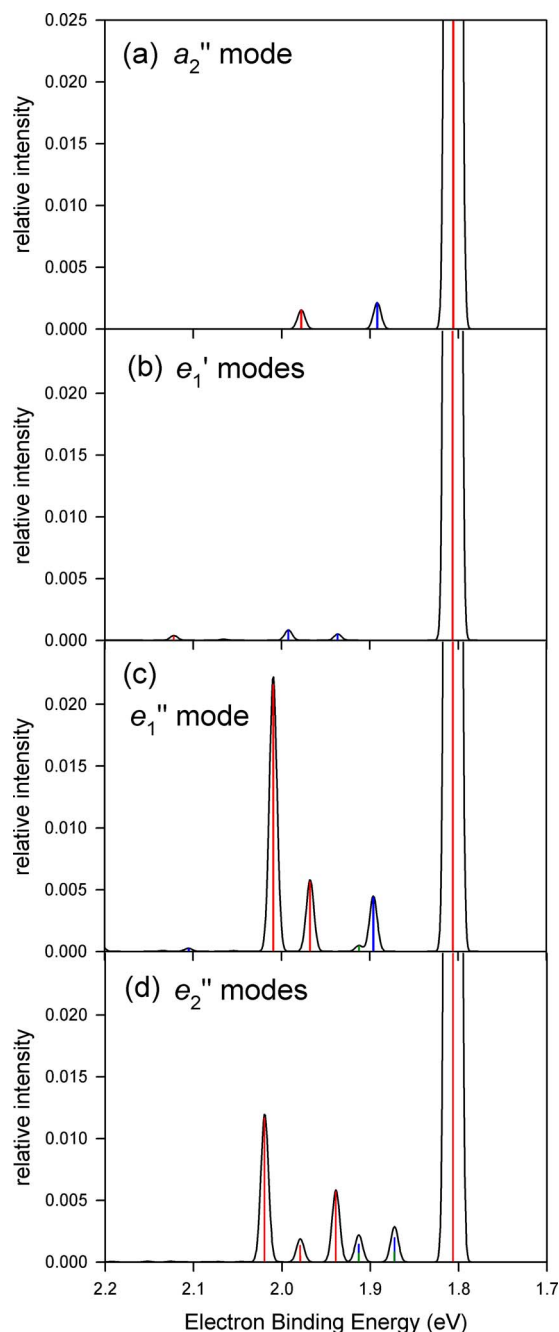


FIG. 8. (Color online) Simulations for the \tilde{X}^2E_1' state of the cyclopentadienyl radical based on the model potential in terms of (a) a_2'' mode accounting for PJT interaction with the \tilde{C}^2E_1' state, (b) e_1' mode accounting for QJT effects and PJT interaction with the \tilde{A}^2A_2'' state, (c) e_1'' mode accounting for QJT effects and PJT interactions with the \tilde{B}^2E_2' , \tilde{D}^2A_1' , and \tilde{E}^2E_2' states, and (d) e_2'' mode accounting for PJT interactions with the \tilde{B}^2E_2' , \tilde{C}^2E_1' , and \tilde{E}^2E_2' states. The sticks represent the positions and relative intensities of individual transitions to vibronic levels of e_1' symmetry (red), (a) e_1' symmetry (blue), (b) a_2'' symmetry (blue), (c) a_1' symmetry (green), e_2' symmetry (blue), (d) e_1' symmetry (green), and e_2' symmetry (blue). The solid lines are the simulated spectra with a Gaussian convolution of a 10 meV full width at half maximum. The intensity scale has been chosen to emphasize weak peaks. The intensity of the origin peak has been set to unity in each simulated spectrum.

(for e_1' vibronic levels) or p wave (e_2' vibronic levels). In the latter case, however, the outgoing p wave is not orthogonal to the transition moment, meaning that both types of levels should be more prominent in the 0° spectrum. Thus, this

simple zeroth-order picture of the detachment process⁷¹ is precisely consistent with what is observed experimentally.⁷² In passing, we note that the fundamental level of the other e_2'' mode (ν_{13}) is not apparent in the experimental spectrum. However, it is possible that ν_{13} is responsible for the broadening to the higher eBE side of peak *d* in the 0° spectrum, where it would be overlapped with the (diminished) peak *e* (see Fig. 2).

Assignment of the remaining peaks—*h* and *j*—is addressed next. Figure 8 shows that the overtone levels of the e_1'' mode might account for these two peaks. As noted earlier, the vibronic symmetry is e_1'' for the overtone levels. Then, the symmetry arguments for the photodetachment process presented above seem to contradict these assignments because photoelectrons for peaks corresponding to final state levels with e_1'' vibronic symmetry would be substantially suppressed at $\theta=0^\circ$. However, it is important to recognize that these two levels have a mixture of a_1' and e_2' vibrational symmetries owing to the QJT coupling and PJT coupling between the \tilde{X}^2E_1' and \tilde{D}^2A_1' states [see EPAPS (Ref. 43)]. This perturbation alters the character of the corresponding wave functions such that the photoelectron angular distributions for these vibronic levels might be significantly different from those for the vibrational ground level. More discussion on this issue is provided later when the wave functions are explored.

Table I summarizes the assignment of the peaks observed in the photoelectron spectrum.

IV. DISCUSSION

A. Nonadiabatic effects in the cyclopentadienyl radical

The success of the simulation of the magic angle photoelectron spectrum of $C_5H_5^-$ (Fig. 5) is attributed to the soundness of the theoretical model. It is important to note that the quadratic model potentials of Eqs. (2) and (3) have been parametrized *ab initio* without any adjustments. Since the parametrization has been performed with the EOMIP-CCSD method, which treats nonadiabatic systems without the artificial effects that often plague quantum-chemical methods,³³ it is safe to conclude that the model potential technique is able to qualitatively describe the essentials of the photodetachment process. The same conclusion was reached in our previous study of the pyrazolyl radical.⁴ The success of these two studies attests to the wide applicability of the quadratic model potential technique.

The present study can be compared with the analyses of other JT systems reported in the literature. Eiding *et al.*⁷³ analyzed the photoelectron spectrum of benzene (C_6H_6) using a linear vibronic coupling model. The LJT coupling constants for the \tilde{X}^2E_{1g} state of the benzene radical cation ($C_6H_6^+$) were calculated at the vertical geometry using the Green's function method.⁷⁴ A simulation based on the linear model potential reproduces the observed spectrum very well, which suggests that BLJT effects in \tilde{X}^2E_{1g} $C_6H_6^+$ are negligible.⁷⁵

In contrast to \tilde{X}^2E_{1g} $C_6H_6^+$, an important BLJT effect

appears to be operative in \tilde{X}^2E CH₃O. Höper *et al.*⁷⁶ parametrized the model potential for \tilde{X}^2E CH₃O up to cubic terms with multireference configuration interaction calculations. Subsequently, Schmidt-Klügmann *et al.*⁷⁷ studied the photoelectron spectrum of CH₃O⁻ with this model potential modified to incorporate spin-orbit coupling. In addition to LJT and QJT couplings, they found that there are also significant effects of BLJT coupling in the spectral simulation. A recent high-resolution photoelectron imaging spectrum of CH₃O⁻ allows more direct assessment of the BLJT effects.⁵⁹

In general, PJT effects on degenerate electronic states have been studied and reported in the literature.^{8,44,78–86} The PJT interactions in \tilde{X}^2E_1' C₅H₅ explored in the present study belong to a particular case where the PJT-active modes are different from the LJT-active modes for the degenerate state. Such a case has also been studied in C₆H₆⁺.^{82,84,85} As mentioned in Sec. I, Miller and co-workers^{26,27} investigated the vibronic structure of \tilde{X}^2E_1' C₅H₅ observed in the dispersed fluorescence spectrum. Among the excited states of C₅H₅ shown in Fig. 7, only the \tilde{D}^2A_1' state can have a nonzero transition dipole moment with the \tilde{A}^2A_2'' state, and the fluorescence spectrum does not show any sign of the fundamental level of a_1' vibronic symmetry.²⁷ On the surface, this suggests that PJT effects are negligible in the fluorescence spectrum and is consistent with the theoretical treatment of Refs. 26 and 27, in which PJT couplings were neglected. However, the omission of PJT effects in the C₅H₅ system can indirectly affect analyses of the fluorescence spectrum with respect to the out-of-plane modes. This possibility is addressed in Sec. IV C.

B. LJT vibronic levels

Multimode mixing is a well-known feature for LJT systems.^{8,73,87–89} In this section, the identities of the vibronic levels of \tilde{X}^2E_1' C₅H₅ observed in the photoelectron spectrum are studied through the model potential technique to address multimode effects. Figure 9 displays the results of simulations where each of the modes included in the model Hamiltonian of Eq. (2) is treated separately. Figure 9(a) is the simulation with a model Hamiltonian with respect to the a_1' mode (ν_2) only. This single-mode simulation demonstrates little activity of the a_1' mode, as is expected from its very small intrastate linear coupling constant (Table IV). Figures 9(b)–9(d) illustrate single-mode simulations for the LJT-active e_2' modes, ν_{12} , ν_{11} , and ν_{10} , respectively. Vibrational progressions along these modes are noticeable in these simulated spectra, and their extents depend on the magnitude of the LJT coupling constants (or the coupling strength, κ/ω , see Tables III and IV). These results of the single-mode simulations clearly indicate that simple convolution of these individual simulations would not amount to the simulation based on the model potential of Eq. (2) (Fig. 4) or Eq. (3) (Fig. 5). Thus, multimode effects are important.

Figure 10 displays the vibronic wave functions in terms of the e_2' coordinates for the vibronic levels of $J = \pm 1/2$ in the single-mode LJT systems. Comparison of the vibronic wave functions for each pair of the degenerate levels shows

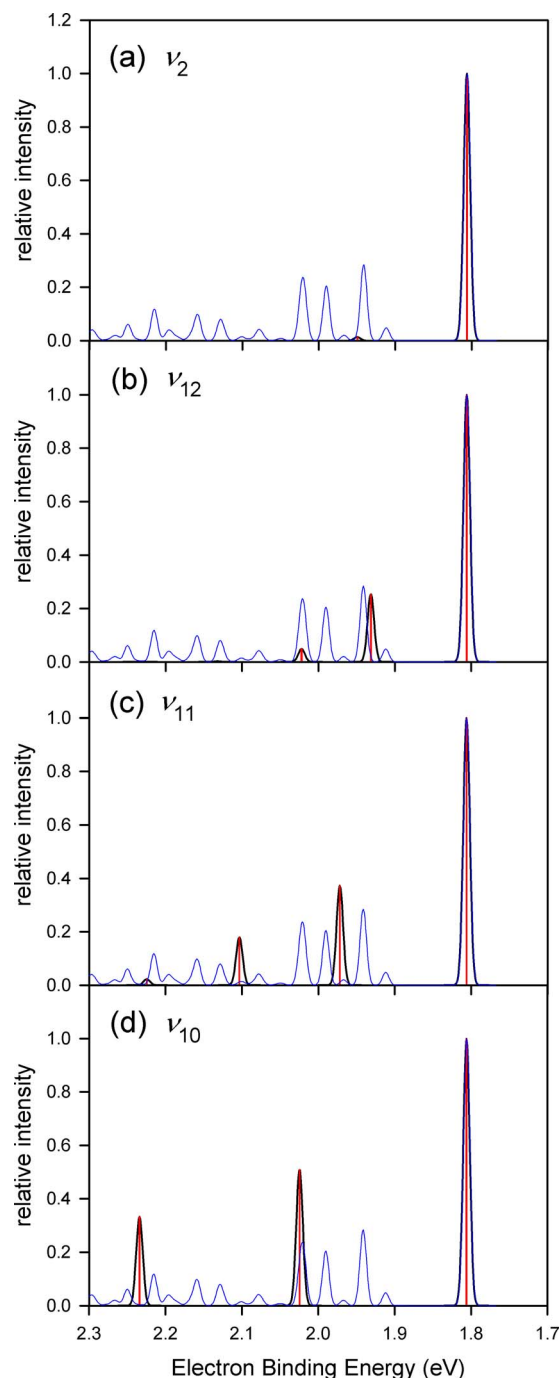


FIG. 9. (Color online) Single-mode simulations for the \tilde{X}^2E_1' state of the cyclopentadienyl radical. The model potential of Eq. (2) has been simplified to take into account (a) only ν_2 mode (a_1'), (b) only ν_{12} mode (e_2'), (c) only ν_{11} mode (e_2'), and (d) only ν_{10} mode (e_2'). The sticks (red) represent the positions and relative intensities of individual transitions to vibronic levels of e_2' symmetry. The black solid line is the simulated spectrum with a Gaussian convolution of a 10 meV full width at half maximum. The simulated spectrum shown in Fig. 5 is reproduced here with the blue solid line for comparison.

that distortion of the equilibrium geometry due to the LJT coupling takes place in the opposite directions for the two degenerate levels [see also Eq. (2)]. The appearance of radial nodes upon vibrational excitation is clearly seen in Fig. 10. On the other hand, the angular node in the vibronic wave function for each of the degenerate levels unambiguously identifies the half-integer angular momentum (i.e., J

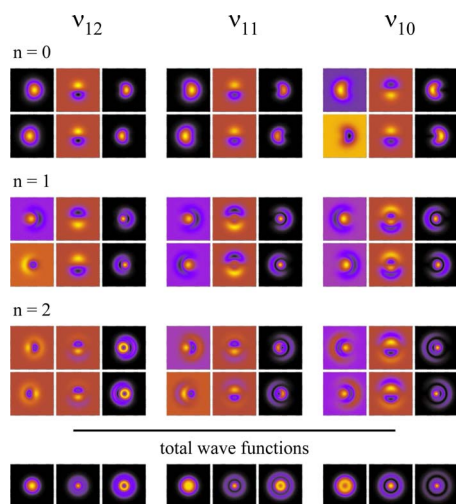


FIG. 10. (Color online) Plots of vibronic wave functions with respect to the e_2' coordinates for the three lowest $J = \pm 1/2$ vibronic levels of single-mode LJT systems. The wave functions have been calculated with the model potentials used for the single-mode simulations shown in Fig. 9. The three main columns correspond to the three e_2' modes: ν_{12} , ν_{11} , and ν_{10} . In each main column, there are three main rows corresponding to the three vibronic levels. For each main row in each main column, a collection of six plots are displayed. In this subset, the upper and lower rows represent the two degenerate vibronic levels. Each of these rows contains three plots. The leftmost and center plots depict the vibrational wave functions for the two degenerate electronic states. The summation of the squares of these two wave functions is shown in the rightmost plot, which corresponds to the square of the vibronic wave function for one of the degenerate vibronic levels. The summation of the squares of the vibronic wave functions for the two degenerate vibronic levels results in the square of the total vibronic wave function for the degenerate vibronic level. These squared total vibronic wave functions are displayed at the bottom of the figure for the three vibronic levels, with the lowest at the leftmost and the highest at the rightmost. In each plot, the horizontal and vertical axes represent the symmetric (with respect to the C_{2v} subgroup) and asymmetric components of the e_2' coordinates, ranging from -5 to 5 in dimensionless units.

$= \pm 1/2$). The total wave function is, of course, totally symmetric, as shown at the bottom of Fig. 10. Figure 10 also exhibits how the vibronic wave functions vary with the strength of the LJT coupling ($|\kappa|/\omega$); ν_{12} has the smallest coupling and ν_{10} has the largest (see Tables III and IV). The single-mode simulations (Fig. 9) and corresponding wave functions (Fig. 10) will be useful as reference points as we discuss multimode JT effects and BLJT effects below.

Vibronic wave functions for $J = \pm 1/2$ levels associated with the multimode model potential of Eqs. (2) and (3) are depicted in Figs. 11 and 12. In these figures, we show the graphical representations (see the figure caption for details) of the states that correspond to peaks *a*, *e*, *f*, *g*, *i*, and *k* in the laboratory spectrum (see Fig. 5). Comparing the wave functions with those obtained in the simple single-mode simulations shown in Fig. 10 is illustrative and demonstrates extensive multimode character in the spectroscopic states. While the wave functions for peak *a* can be trivially interpreted as the vibrational origin, those of the higher states reveal extensive mode mixing. First, the lowest excited $J = \pm 1/2$ level is seen to involve a fair degree of (out-of-phase) mixing between ν_{12}^1 and ν_{11}^1 , a finding which is consistent with a fairly significant redshift from the position of ν_{12}^1 in the single-mode simulation [see Fig. 9(b)]. Mixing with ν_{10}^1 is rather less apparent (cf. Fig. 10), as expected on simple consider-

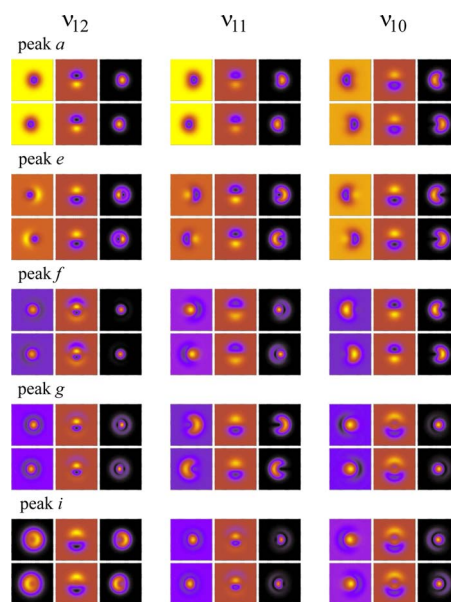


FIG. 11. (Color online) Plots of vibronic wave functions with respect to the e_2' coordinates for $J = \pm 1/2$ vibronic levels calculated with the model potentials of Eqs. (2) and (3). The corresponding simulation is shown in Fig. 5. See Fig. 10 caption for explanation of the plots. For all the plots, the wave functions have been calculated at the minimum of the adiabatic potential energy surface (i.e., integrated along the bottom of the pseudorotation path).

ations of energy separations of the uncoupled levels (see Fig. 9). Peak *f* involves mostly ν_{11}^1 among the e_2' modes, but Fig. 13, which shows the projections of the wave functions along the ν_2 mode, indicates that the bilinear coupling between ν_2 and ν_{11} is significant for this feature: The vibronic wave function clearly contains a contribution from ν_2^1 . This, again, is consistent with expectations of perturbation theory, as the fundamental level of ν_2 in the single-mode simulation is

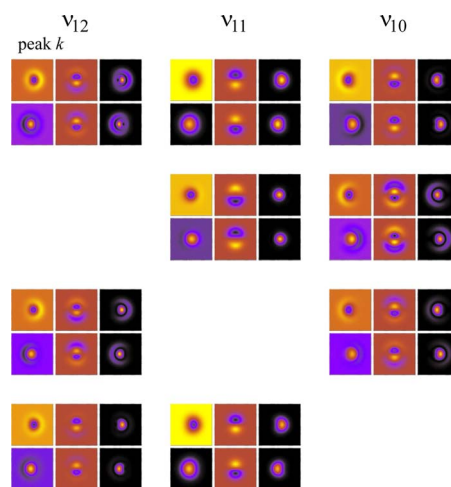


FIG. 12. (Color online) Plots of vibronic wave functions with respect to the e_2' coordinates for a $J = \pm 1/2$ vibronic level calculated with the model potentials of Eqs. (2) and (3). The corresponding simulation is shown in Fig. 5. This vibronic level corresponds to peak *k*. See Fig. 10 caption for explanation of the plots. For the top main row, the wave functions have been calculated at the minimum of the adiabatic potential energy surface (i.e., integrated along the bottom of the pseudorotation path). For the remaining three main rows, integration over one of the three e_2' coordinates has been performed with a radial shift of one dimensionless unit off the minimum. These particular modes are ν_{12} (the second main row), ν_{11} (the third), and ν_{10} (the bottom row).

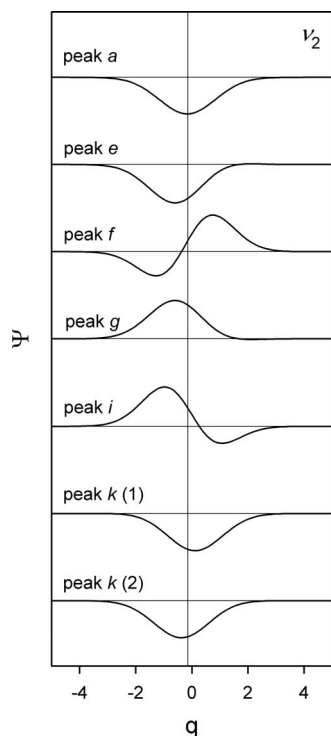


FIG. 13. Plots of vibrational wave functions with respect to the a_1' coordinate (ν_2) for $J = \pm 1/2$ vibronic levels calculated with the model potentials of Eqs. (2) and (3). The corresponding simulation is shown in Fig. 5. The plots correspond to the wave functions for one of the degenerate states, but the identical wave functions have been obtained for the other state (with possible phase reversal). The wave functions have been calculated at the minimum of the adiabatic potential energy surface (i.e., integrated along the bottom of the pseudorotation path). The vertical line indicates the position of the adiabatic potential energy minimum.

close to peak f energetically. It should be recalled that inclusion of the bilinear couplings in the model potential results in a significant enhancement in the intensity of peak f (cf. Figs. 4 and 5). Both peaks g and i have significant contributions from ν_{10}^1 . The former appears to mix to a slight degree with ν_{11}^1 and the overtone ν_{12}^2 . The latter is yet more strongly mixed with contributions from ν_{11}^2 , ν_{12}^1 , and ν_{12}^2 ; in addition, Fig. 13 shows that bilinear coupling acts to mix some ν_2^1 into this transition as well.

Peak k warrants a somewhat more complicated analysis. In the simulation shown in Fig. 5, it appears that peak k comprises two different vibronic transitions. These levels are now dominated by two-quantum transitions and necessitate a slightly different graphical representation. Those in Fig. 11, used in the analysis above, are shown relative to the minimum energy geometry. Accordingly, Fig. 12, which represents one of the two levels corresponding to peak k , also displays calculations in which integration over one of the three e_2' coordinates is performed with a radial shift of one dimensionless unit off the minimum. The wave functions for the other level (lower in energy) are provided in the EPAPS document.⁴³ These vibronic wave functions reveal that the following characters make up the lower level: ν_{10}^1 , ν_{11}^1 , ν_{11}^2 , $\nu_{11}^1 + \nu_{12}^1$, and ν_{12}^2 . The upper level mostly displays the character of $\nu_{10}^1 + \nu_{11}^1$, $\nu_{10}^1 + \nu_{12}^1$, $\nu_{11}^1 + \nu_{12}^1$, ν_{12}^1 , and ν_{12}^2 .

It is apparent from the above analysis that, while the lowest vibronic levels lend themselves to a relatively unam-

TABLE IX. Comparison of LJT coupling constants (κ , eV) and the corresponding harmonic frequencies (ω , cm^{-1}): $D = \frac{1}{2}(\kappa/\omega)^2$; dimensionless.

		This work		Dispersed fluorescence study ^a	
		EOMIP-CCSD/DZP	Spectral fitting	CASSCF/6-31G*	
ν_{10}	$ \kappa $	0.2125	0.14	0.20	
	ω	1434	1320	1411	
	D	0.7147	0.36	0.68	
ν_{11}	$ \kappa $	0.1149	0.14	0.11	
	ω	1063	1041	1058	
	D	0.3800	0.57	0.34	
ν_{12}	$ \kappa $	0.0626	0.067	0.062	
	ω	834	872	815	
	D	0.1831	0.19	0.19	

^aReference 27.

biguous description in terms of quantum numbers (peak $a \leftrightarrow 0-0$; peak $e \leftrightarrow \nu_{12}^1$; and peak $f \leftrightarrow \nu_{11}^1$), the extent of mode mixing grows quite rapidly with the level position. One can easily conclude that levels above peak k will be so highly scrambled as to completely defy efforts to describe them in simple terms. This remark can also be appreciated from the point of view of conical intersections. The model potential used in this work yields a LJT stabilization energy of 0.1961 eV, while BLJT effects only slightly change the stabilization energy to 0.1937 eV.⁹⁰ Thus, peak k , which is predicted to be 0.218 eV above the ground vibronic level, is already past the onset of the extremely complicated level structure and dynamics above the intersection. Thus levels near and above k are expected to exhibit profound nonadiabatic character.

C. Comparison with fluorescence spectrum

Dispersed fluorescence spectra measured by Applegate *et al.*²⁷ reveal a rich vibronic structure in $\tilde{X}^2E_1'' C_5H_5$. They analyzed the spectra based on a linear vibronic coupling model and concluded that some of the vibronic levels are directly associated with LJT effects and the others are vibronic levels of out-of-plane modes. In this section, the results of our photoelectron spectroscopic study are compared with their somewhat complementary dispersed fluorescence study²⁷ in an attempt to broaden our knowledge of the vibronic structure of $\tilde{X}^2E_1'' C_5H_5$.

Table IX compares the LJT coupling constants determined in the present study with those of Ref. 27. In the fluorescence study, LJT coupling constants were first evaluated with *ab initio* calculations and then adjusted to optimize the spectral fit.^{26,27} This refinement procedure yielded coupling constants that are quite different from the *ab initio* values, as seen in Table IX. Interestingly, the coupling constants obtained in their CASSCF/6-31G* calculations²⁶ are close to those determined from EOMIP-CCSD/DZP calculations in the present study. On the other hand, the adjusted values determined from the spectral fitting are often significantly different from the pure *ab initio* values. This deserves attention since our *ab initio* constants apparently describe the photoelectron spectrum so well, and one would expect that

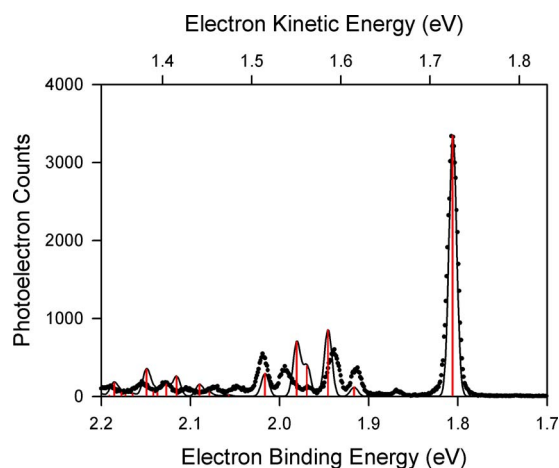


FIG. 14. (Color online) A simulation for the \tilde{X}^2E_1' state of the cyclopentadienyl radical based on the model potential of Eq. (2) accounting for LJT effects, but the coupling constants of the model potential have been taken from Ref. 27. The a_1' mode is excluded from the model potential. The sticks (red) represent the positions and relative intensities of individual transitions to vibronic levels of e_1' symmetry. The solid line is the simulated spectrum with a Gaussian convolution of a 10 meV full width at half maximum, superimposed on the experimental spectrum (dots).

the set of constants describing the dispersed fluorescence spectrum would not differ substantially.

In order to analyze the effects of the different sets of coupling constants, we have used the empirical values of LJT coupling constants from Ref. 27 in the model potential of Eq. (2) to simulate the photoelectron spectrum. The results are shown in Fig. 14. While the corresponding LJT simulation based on the model potential parametrized with EOMIP-CCSD calculations (Fig. 4) at least reproduces the peak positions very well, the empirical model potential of Ref. 27 worsens the quality of the simulation significantly.

As mentioned earlier, a main challenge posed in the analysis of the fluorescence spectrum is to differentiate the peaks directly associated with the LJT effects from those representing out-of-plane modes. Moreover, it is not necessarily straightforward to assign vibronic levels of the out-of-plane modes per se. Below, we focus on the vibronic structure of \tilde{X}^2E_1' C_5H_5 with respect to the out-of-plane modes.

In the dispersed fluorescence spectrum,²⁷ the most intense peak besides the origin peak is located at 1531 cm^{-1} and was identified as the overtone peak of the e_1' mode (ν_8^2). The authors noted a large difference in the quadratic force constant of ν_8 between the initial (\tilde{A}^2A_2'') and final (\tilde{X}^2E_1') states evaluated with the CASSCF calculations,²⁶ which acts to rationalize the apparently substantial intensity for the overtone peak.

The CASSCF calculations of Ref. 26 find a D_{5h} structure for \tilde{A}^2A_2'' C_5H_5 , but the adiabatic EOMIP-CCSD calculations of the present work lead to a different conclusion. The EOMIP-CCSD calculations find an imaginary frequency of $512i\text{ cm}^{-1}$ for the e_1' mode under D_{5h} symmetry. Analytic λ calculations find a large linear interstate coupling constant of 0.36 eV between the \tilde{A}^2A_2'' and \tilde{C}^2E_1' states (see Fig. 7), which explains the imaginary frequency for the lower \tilde{A}^2A_2'' state. Indeed, modest to large vibronic couplings between the

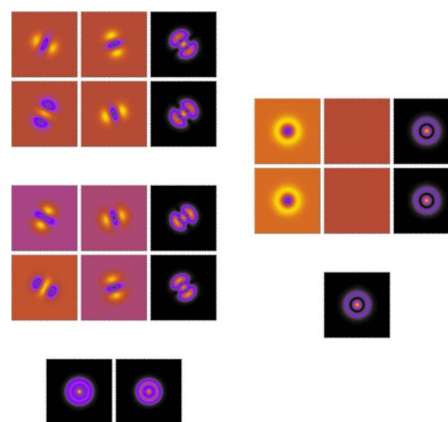


FIG. 15. (Color online) (Left) Plots of vibronic wave functions with respect to the e_1' coordinates for the overtone sublevels of e_1' vibronic symmetry calculated with the corresponding model potential. The corresponding simulation is shown in Fig. 8(c). See Fig. 10 caption for explanation of the plots. (Right) Plots of vibronic wave functions for one of the overtone levels of e_2'' vibronic symmetry calculated with the corresponding model potential. The corresponding simulation is shown in Fig. 8(d).

\tilde{A}^2A_2'' state and each of the higher excited states shown in Fig. 7 have been found in our analytic λ calculations. These vibronic couplings considerably perturb the adiabatic potential energy surface of the \tilde{A}^2A_2'' state along the out-of-plane normal coordinates.⁹¹ Nevertheless, we concur with the assignment of 1531 cm^{-1} as ν_8^2 , but note that the present photoelectron spectroscopic study strongly suggests that the splitting of this e_1' overtone level should be taken into account in the fluorescence spectrum. In Sec. III C, we have assigned peaks *h* and *j* as the vibronic sublevels of ν_8^2 . The position of peak *j* matches the corresponding assignment in the fluorescence spectrum (see Table I).

Further support for this assignment comes from the nature of the wave functions of the vibronic levels. Figure 15 illustrates the wave functions of the e_1' overtone sublevels calculated with the corresponding model potential. Radial nodes in the wave functions expose their identity as the overtone level. Also noticeable are angular nodes in the wave functions for the pair of the degenerate levels. These angular nodes are absent, for instance, in the wave functions for the overtone levels of the e_2'' modes. The wave function for one of the e_2'' overtone levels has been calculated with the corresponding model potential and depicted in Fig. 15. Thus, the character of the wave functions for the overtone level is quite different between the e_1' and e_2'' modes. This difference originates from nonadiabatic interactions, as explained in the EPAPS document.⁴³

The difference in the angular character of the overtone-level wave functions between the e_1' and e_2'' modes most probably gives rise to different angular distributions of the corresponding photoelectrons. As a result, the peaks for the overtone sublevels of the e_1' mode appear to be relatively enhanced in the 0° photoelectron spectrum [Fig. 2(b)].

The discussion presented above leads to the conclusion that, while the intense peak at 1531 cm^{-1} in the fluorescence spectrum certainly represents one of the e_1' overtone sublevels, the other e_1' overtone sublevel has yet to be assigned in

TABLE X. Vibronic levels of the \tilde{X}^2E_1' state of the cyclopentadienyl radical.

Photoelectron spectroscopy ^a	Dispersed fluorescence ^b	Simulation ^a	Previous assignment ^b	Present assignment ^{a,c}
0	0	0	Ground level	Ground level (e_1'')
	457	455	$J = \pm 3/2, 1$	$J = \pm 3/2, 1(e_1'')$
500 ± 7				$\nu_{14}^1 (e_1' + e_2')$
657 ± 20				$\nu_4^1 (e_1')$
778 ± 20				$\nu_8^1 (e_2')$
875 ± 12	870	856	$J = \pm 1/2, 1$	$J = \pm 1/2, 1(e_1'')$
	919	887	$J = \pm 3/2, 2$	$J = \pm 3/2, 2(e_1'')$
1078 ± 10	1071	1093	ν_2^1	$J = \pm 1/2, 2(e_1'')$
	1130	1141	$J = \pm 1/2, 2$	$J = \pm 1/2, 3(e_1'')$
	1151		ν_{14}^2	$\nu_4^1 + \nu_{14}^1 (e_1'')$
	1212	1200	$J = \pm 3/2, 3$	$J = \pm 3/2, 3(e_2'')$
	1244		ν_3^1	$\nu_8^1 + \nu_{14}^1 (e_1'')$
1313 ± 21	1306	1301	$J = \pm 1/2, 3$	$J = \pm 1/2, 4(e_1'')$
1379 ± 17	1361		ν_4^2	$\nu_8^2 (e_1'')$
	1409		$J = \pm 1/2, 4$	$\nu_{13}^1 + \nu_{14}^1 (e_1'')$
	1434		$\nu_{13}^1 + \nu_{14}^1$	$J = \pm 3/2, 1 + \nu_{14}^2 (e_1'')$
1512 ± 14		1488		$J = \pm 1/2, 5(e_1'')$
1533 ± 15	1531		ν_8^2	$\nu_8^2 (e_1'')$
1716 ± 15	1707	1723	$J = \pm 1/2, 5$	$J = \pm 1/2, 6(e_1'')$
	1721	1756	ν_{13}^2	$J = \pm 1/2, 7(e_1'')$
				$\nu_8^1 + \nu_{13}^1 (e_1'')$
	1926		$J = \pm 1/2, 1 + \nu_2^1$	$\nu_{13}^2 (e_1'')$

^aPresent study.^bReference 27.^cNote that bilinear coupling effectively mixes the a_1' and e_2' modes and these modes are not differentiated in the present assignments.

the fluorescence spectrum. Indeed, a peak at 1361 cm^{-1} in the fluorescence spectrum (which is very close to the position of peak *h* in the photoelectron spectrum) was assigned as the overtone level of the a_2'' mode (ν_4) in Ref. 27. This assignment is plausible but the alternative assignment to a sublevel of ν_8^2 should also be considered, given the findings of our research.

Another issue bearing on the assignment of peaks for out-of-plane modes is concerned with anharmonic coupling. The JT distortion that turns the equilibrium geometry of \tilde{X}^2E_1' to C_{2v} provides anharmonic coupling which can mix the e_2'' modes with the a_2'' and e_1'' modes in the \tilde{X}^2E_1' state. These anharmonic effects can be very important in the fluorescence spectrum because of the relatively large overtone excitation of both the e_1'' and e_2'' modes, which reflects strong PJT interaction in the \tilde{A}^2A_2'' state along these coordinates. These anharmonic effects can be neglected in the analysis of the photoelectron spectrum of $C_5H_5^-$ because only very weak intensity is found for the overtone levels of out-of-plane modes in the \tilde{X}^2E_1' state.

The peak positions measured in the present photoelectron spectroscopic study and those measured in the previous dispersed fluorescence study²⁷ are compared in Table X. Based on the model potential analysis in the present study and discussions laid out above, some additional plausible assignments are suggested in Table X. In a subsequent work, we will present a more thorough analysis based on full-scale simulations of the dispersed fluorescence spectrum with our vibronic Hamiltonian.⁹²

D. Thermochemistry

A variety of environmental concerns have led to a significant number of studies of hydrocarbon combustion chemistry in recent years.^{93–96} The formation of small aromatic species such as benzene in hydrocarbon combustion has been a subject of intense study as they may be closely linked to the development of polycyclic aromatic hydrocarbons and, subsequently, soot. It is known that the C_5H_5 radical is an important intermediate in the chemistry of benzene and naphthalene in combustion environments.^{97–100} The radical is generated in the oxidation of benzene, thus playing an important role in regeneration of six-membered aromatic species.^{101–109} Since investigation of combustion chemistry usually has to rely on some types of kinetic model, thermodynamic data of reactive species are valuable in this research field.

Several values of the standard enthalpy of formation of C_5H_5 have been reported in the literature. Furuyama *et al.*¹¹⁰ studied the kinetics of a cyclopentadiene (C_5H_6) and iodine system and derived a standard enthalpy of formation of C_5H_5 at 298 K, $\Delta_f H_{298}(C_5H_5) = 60.9 \pm 1.2 \text{ kcal mol}^{-1}$, from the analysis of a kinetic model. DeFrees *et al.*¹¹¹ measured the proton affinity of C_5H_5 with ion cyclotron double resonance spectroscopy and determined $\Delta_f H_{298}(C_5H_5) = 63.2 \pm 2.2 \text{ kcal mol}^{-1}$ from a positive ion thermochemical cycle. Kern *et al.*¹¹² explored the pyrolysis of C_5H_6 with time-of-flight mass spectroscopy and laser-schlieren densitometry and estimated $\Delta_f H_{298}(C_5H_5) = 65.3 \text{ kcal mol}^{-1}$ from the analysis of a kinetic model. Roy *et al.*^{113,114} measured the forward and reverse reaction rate coefficients for the C–H

bond dissociation of C_5H_6 with atomic resonance absorption spectroscopy and determined $\Delta_f H_{298}(C_5H_5) = 62.5 \pm 1.0$ kcal mol⁻¹ from a “third law” analysis. Nunes *et al.*¹¹⁵ estimated $\Delta_f H_{298}(C_5H_5) = 64.8 \pm 1.9$ kcal mol⁻¹ from the electronic structure calculations and their time-resolved photoacoustic calorimetry measurements in benzene solution. This survey reveals that various results spread over a range of nearly 7 kcal mol⁻¹, a significant spread, especially when the importance of C_5H_5 is considered.

The present study offers an independent determination of the thermochemical quantities of C_5H_5 by utilizing a negative ion thermochemical cycle,¹¹⁶

$$D_0(C_5H_6, C-H) = \Delta_{acid}H_0(C_5H_6) + EA(C_5H_5) - IE(H). \quad (5)$$

Here, $D_0(C_5H_6, C-H)$ and $\Delta_{acid}H_0(C_5H_6)$ are the C–H bond dissociation energy (BDE) and the 0 K C–H deprotonation enthalpy, respectively, of cyclopentadiene, $EA(C_5H_5)$ is the EA of the cyclopentadienyl radical, and $IE(H)$ is the ionization energy of the hydrogen atom (13.598 44 eV).¹¹⁷ In an earlier photoelectron spectroscopic study¹⁸ of $C_5H_5^-$, the ion was generated in a hot, low pressure ion source and the electron energy analyzer had quite poor resolution. In the present study, both of these limitations have been significantly reduced, resulting in a fourfold reduction in the error associated with the EA determination.

The relative gas-phase acidity of C_5H_6 is available from the literature.¹¹⁸ Updated acidity data for the reference systems^{1,2} yield the gas-phase acidity of C_5H_6 ; $\Delta_{acid}G_{298}(C_5H_6) = 348.3 \pm 1.1$ kcal mol⁻¹. An entropy correction can be made to the acidity using data obtained from the electronic structure calculations to derive the 298 K C–H deprotonation enthalpy: $\Delta_{acid}H_{298}(C_5H_6) = 355.0 \pm 1.2$ kcal mol⁻¹. An integrated heat capacity is estimated similarly to derive $\Delta_{acid}H_0(C_5H_6) = 353.4 \pm 1.3$ kcal mol⁻¹.

These thermochemical data are combined in Eq. (5) to determine the C–H BDE of C_5H_6 : $D_0(C_5H_6, C-H) = 81.5 \pm 1.3$ kcal mol⁻¹. This BDE is in good agreement with the value determined by Roy *et al.* (80.8 ± 1.0 kcal mol⁻¹).¹¹⁴ A temperature correction leads to the 298 K bond enthalpy: $D_{298}(C_5H_6, C-H) = 83.4 \pm 1.3$ kcal mol⁻¹. With $\Delta_f H_{298}(C_5H_6) = 31.9 \pm 0.4$ kcal mol⁻¹,¹¹⁰ a temperature-corrected value, $\Delta_f H_0(C_5H_6) = 36.0 \pm 0.5$ kcal mol⁻¹, and the corresponding values for the H atom,¹¹⁹ we obtain the standard enthalpy of formation of C_5H_5 : $\Delta_f H_{298}(C_5H_5) = 63.2 \pm 1.4$ kcal mol⁻¹ and $\Delta_f H_0(C_5H_5) = 65.9 \pm 1.4$ kcal mol⁻¹. These values are in good agreement with those determined by Roy *et al.*¹¹⁴ and DeFrees *et al.*¹¹¹ In summary, the thermochemical data determined in the present study do not radically modify the accepted thermochemical properties of C_5H_5 but reduce the uncertainty and add significantly to the confidence with which they may be employed in kinetic models of combustion.

V. CONCLUSION

The photoelectron spectrum of $C_5H_5^-$ reveals the vibronic structure of $\tilde{X}^2E_1'' C_5H_5$. A model potential for $\tilde{X}^2E_1'' C_5H_5$ has been constructed based on EOMIP-CCSD/DZP calculations to account for the LJT effects along the e_2' coordinates as well as the BLJT effects along the a_1' and e_2' coordinates. A simulation of the photoelectron spectrum based on the *ab initio* model potential reproduces the magic angle spectrum very well, helping to elucidate the complicated nonadiabatic effects in $\tilde{X}^2E_1'' C_5H_5$. Identification of the vibronic levels of $J = \pm 1/2$ is facilitated by calculations of their vibronic wave functions, which reveal JT as well as BLJT mode mixings.

A number of weak peaks associated with out-of-plane modes in $\tilde{X}^2E_1'' C_5H_5$ appear distinctly in the 0° photoelectron spectrum. Nonadiabatic couplings of the \tilde{X}^2E_1'' state with the electronic excited states have been evaluated analytically with EOMIP-CCSD calculations. The assignments of these peaks have been made through the simulation based on the model potentials, which take into account these PJT interactions as well as QJT interactions in the \tilde{X}^2E_1'' state. The results of the present study are compared with those of a previous dispersed fluorescence study by Miller and co-workers^{26,27} to better understand the vibronic structure of $\tilde{X}^2E_1'' C_5H_5$.

The EA of C_5H_5 has been determined to be 1.808 ± 0.006 eV. This EA value is utilized in a negative ion thermochemical cycle to determine the C–H BDE of C_5H_6 to be $D_0(C_5H_6, C-H) = 81.5 \pm 1.3$ kcal mol⁻¹. Using this result, the standard enthalpy of formation of C_5H_5 has been determined with greater accuracy than was possible previously: $\Delta_f H_{298}(C_5H_5) = 63.2 \pm 1.4$ kcal mol⁻¹ and $\Delta_f H_0(C_5H_5) = 65.9 \pm 1.4$ kcal mol⁻¹.

ACKNOWLEDGMENTS

We would like to thank Dr. Jeffery Rathbone for his help in understanding the vibronic structure of the cyclopentadienyl radical. Portions of electronic structure calculations and model potential calculations were performed with the JILA Keck Cluster supported by the W. M. Keck Foundation. This research was funded by the Air Force Office of Scientific Research, the National Science Foundation, the Department of Energy, and the Welch Foundation.

¹A. J. Gianola, T. Ichino, R. L. Hoenigman, S. Kato, V. M. Bierbaum, and W. C. Lineberger, *J. Phys. Chem. A* **108**, 10326 (2004).

²A. J. Gianola, T. Ichino, R. L. Hoenigman, S. Kato, V. M. Bierbaum, and W. C. Lineberger, *J. Phys. Chem. A* **109**, 11504 (2005).

³A. J. Gianola, T. Ichino, S. Kato, V. M. Bierbaum, and W. C. Lineberger, *J. Phys. Chem. A* **110**, 8457 (2006).

⁴T. Ichino, A. J. Gianola, W. C. Lineberger, and J. F. Stanton, *J. Chem. Phys.* **125**, 084312 (2006).

⁵T. Ichino, A. J. Gianola, S. Kato, V. M. Bierbaum, and W. C. Lineberger, *J. Phys. Chem. A* **111**, 8374 (2007).

⁶S. M. Villano, A. J. Gianola, N. Eyet, T. Ichino, S. Kato, V. M. Bierbaum, and W. C. Lineberger, *J. Phys. Chem. A* **111**, 8579 (2007).

⁷T. Ichino, D. H. Andrews, G. J. Rathbone, F. Misaizu, R. M. D. Calvi, S. W. Wren, S. Kato, V. M. Bierbaum, and W. C. Lineberger, *J. Phys. Chem. B* **112**, 545 (2008).

- ⁸H. Köppel, W. Domcke, and L. S. Cederbaum, *Adv. Chem. Phys.* **57**, 59 (1984).
- ⁹This degenerate state correlates with the aforementioned \tilde{X}^2A_2 and \tilde{A}^2B_1 states in pyrazolyl.
- ¹⁰R. Englman, *The Jahn-Teller Effect in Molecules and Crystals* (Wiley, London, 1972).
- ¹¹B. A. Thrush, *Nature (London)* **178**, 155 (1956).
- ¹²W. D. Hobey and A. D. McLachlan, *J. Chem. Phys.* **33**, 1695 (1960).
- ¹³A. D. Liehr, *J. Phys. Chem.* **67**, 389 (1963).
- ¹⁴G. R. Liebling and H. M. McConnell, *J. Chem. Phys.* **42**, 3931 (1965).
- ¹⁵G. Porter and B. Ward, *Proc. R. Soc. London, Ser. A* **303**, 139 (1968).
- ¹⁶R. Engleman, Jr. and D. A. Ramsay, *Can. J. Phys.* **48**, 964 (1970).
- ¹⁷J. H. Richardson, L. M. Stephenson, and J. I. Brauman, *J. Chem. Phys.* **59**, 5068 (1973).
- ¹⁸P. C. Engelking and W. C. Lineberger, *J. Chem. Phys.* **67**, 1412 (1977).
- ¹⁹W. T. Borden and E. R. Davidson, *J. Am. Chem. Soc.* **101**, 3771 (1979).
- ²⁰H. H. Nelson, L. Pasternack, and J. R. McDonald, *Chem. Phys.* **74**, 227 (1983).
- ²¹L. Yu, S. C. Foster, J. M. Williamson, M. C. Heaven, and T. A. Miller, *J. Phys. Chem.* **92**, 4263 (1988).
- ²²L. Yu, J. M. Williamson, and T. A. Miller, *Chem. Phys. Lett.* **162**, 431 (1989).
- ²³R. N. McDonald, E. J. Bianchina, Jr., and C. C. Tung, *J. Am. Chem. Soc.* **113**, 7115 (1991).
- ²⁴L. A. Yu, D. W. Cullin, J. M. Williamson, and T. A. Miller, *J. Chem. Phys.* **98**, 2682 (1993).
- ²⁵M. J. Bearpark, M. A. Robb, and N. Yamamoto, *Spectrochim. Acta, Part A* **55**, 639 (1999).
- ²⁶B. E. Applegate, T. A. Miller, and T. A. Barckholtz, *J. Chem. Phys.* **114**, 4855 (2001).
- ²⁷B. E. Applegate, A. J. Bezant, and T. A. Miller, *J. Chem. Phys.* **114**, 4869 (2001).
- ²⁸T. Sato, K. Tokunaga, and K. Tanaka, *J. Chem. Phys.* **124**, 024314 (2006).
- ²⁹F. Sicilia, L. Blancafort, M. J. Bearpark, and M. A. Robb, *J. Phys. Chem. A* **111**, 2182 (2007).
- ³⁰H. C. Longuet-Higgins, U. Öpik, M. H. L. Pryce, and R. A. Sack, *Proc. R. Soc. London, Ser. A* **244**, 1 (1958).
- ³¹H. C. Longuet-Higgins, *Adv. Spectrosc. (N.Y.)* **2**, 429 (1961).
- ³²J. F. Stanton and J. Gauss, *J. Chem. Phys.* **101**, 8938 (1994).
- ³³J. F. Stanton, *J. Chem. Phys.* **115**, 10382 (2001).
- ³⁴G. Herzberg, *Molecular Spectra and Molecular Structure III: Electronic Spectra and Electronic Structure of Polyatomic Molecules* (Van Nostrand, Princeton, 1967).
- ³⁵K. M. Ervin and W. C. Lineberger, in *Advances in Gas Phase Ion Chemistry*, edited by N. G. Adams and L. M. Babcock (JAI, Greenwich, 1992), Vol. 1, p. 121.
- ³⁶D. G. Leopold, K. K. Murray, A. E. Stevens Miller, and W. C. Lineberger, *J. Chem. Phys.* **83**, 4849 (1985).
- ³⁷K. M. Ervin, J. Ho, and W. C. Lineberger, *J. Chem. Phys.* **91**, 5974 (1989).
- ³⁸D. M. Neumark, K. R. Lykke, T. Andersen, and W. C. Lineberger, *Phys. Rev. A* **32**, 1890 (1985).
- ³⁹T. Andersen, H. K. Haugen, and H. Hotop, *J. Phys. Chem. Ref. Data* **28**, 1511 (1999).
- ⁴⁰J. Cooper and R. N. Zare, *J. Chem. Phys.* **48**, 942 (1968).
- ⁴¹The small intensities for peaks *b*, *c*, *d*, *h*, and *j* raise the potential concern that these photoelectrons might originate from impurity ions. Specifically, it has been reported that the reaction of O^- with C_5H_6 yields two major ion products: the cyclopentadienylidene radical anion ($C_5H_4^-$, 52%) and $C_5H_5^-$ (40%) [Y. L. Guo and J. J. Grabowski, *Int. J. Mass Spectrom. Ion Process.* **117**, 299 (1992)]. If this reaction were significantly taking place in the ion source, then $C_5H_4^-$ (*m/z* of 64) might contaminate $C_5H_5^-$ (*m/z* of 65) beam, considering the limited mass resolution of our Wien velocity filter. In our separate measurements, we have observed considerable change in the profile of the photoelectron spectrum when we switch the reactant ion from HO^- to O^- . A relatively intense peak appears at $eBE = 1.750 \pm 0.010$ eV when the reactant ion is O^- . An EA value of 1.751 ± 0.047 eV for cyclopentadienylidene (C_5H_4) has been reported in a previous threshold photodetachment experiment for $C_5H_4^-$ (Ref. 23). In our measurements of the photoelectron spectra of $C_5H_5^-$ reported in this article, an excess amount of methane gas has been introduced into the flow tube to ensure quantitative conversion of O^- to HO^- . The absence of $C_5H_4^-$ in the ion beam can be confirmed by the absence of a peak at 1.75 eV (see particularly Fig. 2).
- ⁴²Note the proximity of the positions of peaks *i* and *j* to each other (see Table I and Fig. 2). The position of peak *i* has been determined from the peak fit in the magic angle spectrum, while that of peak *j* from the peak fit in the 0° spectrum. See also discussion on the photoelectron angular distributions given in Secs. III C 5 and IV C. The proximity makes it impossible to resolve these two peaks in *one* spectrum in the current measurements. Consequently, it is hard to discern the relative contributions of the two vibronic transitions to the peak intensity in Fig. 2(b). However, the different identities of peaks *i* and *j* can be recognized when the *relative* intensities of peaks *f* and *i* in the magic angle spectrum are compared with those of peaks *f* and *j* in the 0° spectrum. The uncertainties of the peak positions shown in Table I originate mainly from the small compression factor of the hemispherical energy analyzer (see Sec. II A). The possible error is *systematic*; it would shift the positions of peaks *i* and *j* (as well as all the other peaks) in the *same* direction.
- ⁴³See EPAPS Document No. E-JCPSA6-129-613834 for supplementary tables, figures and text. For more information on EPAPS, see <http://www.aip.org/pubservs/epaps.html>.
- ⁴⁴J. F. Stanton, *J. Chem. Phys.* **126**, 134309 (2007).
- ⁴⁵G. D. Purvis and R. J. Bartlett, *J. Chem. Phys.* **76**, 1910 (1982).
- ⁴⁶T. H. Dunning, Jr., *J. Chem. Phys.* **53**, 2823 (1970).
- ⁴⁷L. T. Redmon, G. D. Purvis, and R. J. Bartlett, *J. Am. Chem. Soc.* **101**, 2856 (1979).
- ⁴⁸J. F. Stanton, J. Gauss, J. D. Watts, P. G. Szalay, and R. J. Bartlett with contributions from, A. A. Auer, D. B. Bernholdt, O. Christiansen, M. E. Harding, M. Heckert, O. Heun, C. Huber, D. Jonsson, J. Juselius, W. J. Lauderdale, T. Metzroth, C. Michauk, D. P. O'Neill, D. R. Price, K. Ruud, F. Schiffmann, M. E. Varner, and J. Vazquez, and the integral packages MOLEUCLE (J. Almlöf and P. R. Taylor), PROPS (P. R. Taylor), and ABACUS (T. Helgaker, H. J. Aa. Jensen, P. Jørgensen, and J. Olsen). For the current version, see <http://www.aces2.de>
- ⁴⁹J. Gauss and J. F. Stanton, *Chem. Phys. Lett.* **276**, 70 (1997).
- ⁵⁰R. A. Young, Jr. and D. R. Yarkony, *J. Chem. Phys.* **125**, 234301 (2006).
- ⁵¹Ten harmonic oscillator eigenfunctions for each mode (i.e., twenty for each degenerate pair) are used to form the direct product basis functions of the model Hamiltonian. This number also serves as the maximum occupation number for the combination levels of q_x and q_y (see Ref. 88) in order to maintain the degeneracy in the truncated model Hamiltonian. Only transitions from the vibrational ground level of $\tilde{X}^1A_1' C_5H_5^-$ are taken into account in spectral simulations. It is assumed that the transition dipole moment for the photodetachment is independent of the nuclear coordinate, and each final electronic state, which is composed of each diabatic electronic state of C_5H_5 and a scattering state for the departing photoelectron, has equal magnitude of the transition dipole moment. One thousand Lanczos iterations are adequate to achieve convergence for the vibronic levels considered in the present study.
- ⁵²Alternatively, the model potential can be constructed in terms of the vibronic eigenstates of the linear Jahn-Teller angular momentum, as was done in, for instance, Ref. 88. Simulation based on such a model potential gives, of course, results identical to those obtained with a model potential of Eq. (2).
- ⁵³P. Chen, in *Unimolecular and Bimolecular Reaction Dynamics*, edited by C. Y. Ng, T. Baer, and I. Powis (Wiley, New York, 1994).
- ⁵⁴M. Mayer, L. S. Cederbaum, and H. Köppel, *J. Chem. Phys.* **100**, 899 (1994).
- ⁵⁵The magnitudes of the bilinear couplings evaluated at the anion geometry are much less than 1 meV.
- ⁵⁶P. C. Engelking, G. B. Ellison, and W. C. Lineberger, *J. Chem. Phys.* **69**, 1826 (1978).
- ⁵⁷D. L. Osborn, D. J. Leahy, E. H. Kim, E. de Beer, and D. M. Neumark, *Chem. Phys. Lett.* **292**, 651 (1998).
- ⁵⁸T. M. Ramond, G. E. Davico, R. L. Schwartz, and W. C. Lineberger, *J. Chem. Phys.* **112**, 1158 (2000).
- ⁵⁹M. J. Nee, A. Osterwalder, J. Zhou, and D. M. Neumark, *J. Chem. Phys.* **125**, 014306 (2006).
- ⁶⁰Our analytic λ calculations with the EOMIP-CCSD/DZP method give a linear interstate coupling constant of substantial magnitude (0.26 eV) for vibronic interaction between the \tilde{X}^2E and \tilde{A}^2A_1 states of CH_3O . The PJT effects on the adiabatic potential energy surface of $\tilde{X}^2E CH_3O$ have not been mentioned in previous computational studies of the potential energy surface; see Ref. 76 and A. V. Marenich and J. E. Boggs, *J. Chem. Phys.* **122**, 024308 (2005).

- ⁶¹For the appearance of $J = \pm 3/2$ vibronic levels in the emission spectra (see, e.g., S. C. Foster, P. Misra, T.-Y. D. Lin, C. P. Damo, C. C. Carter, and T. A. Miller, *J. Phys. Chem.* **92**, 5914 (1988); A. Geers, J. Kappert, F. Temps, and T. J. Sears, *J. Chem. Phys.* **98**, 4297 (1993)), nuclear coordinate dependence of the transition dipole moment has been considered in Ref. 76.
- ⁶²State labeling of C_5H_5 considers only single-hole states in the present study. It should be mentioned that removal of one electron from an e_1'' orbital accompanied by excitation of another electron from an e_1' orbital to an e_2' orbital lead to dominant configurations of the electronic states of C_5H_5 of A_1' , A_2' , E_1'' , and E_2'' symmetries. EOMEE-CCSD calculations suggest that these two-hole-one-particle doublet states ("satellite" states) lie about 6 eV higher in energy than the \tilde{X}^2E_1'' state. Since the cross sections for photodetachment to these satellite states are typically very small, it is reasonable to neglect nonadiabatic interaction with these satellite states regarding nonadiabatic peaks in the \tilde{X}^2E_1'' state. Such satellite states have been observed in the Penning ionization electron spectrum [S. Masuda, M. Aoyama, K. Ohno, and Y. Harada, *Phys. Rev. Lett.* **65**, 3257 (1990); T. Takami and K. Ohno, *J. Chem. Phys.* **96**, 6523 (1992)]; and photoelectron spectrum of benzene [P. Baltzer, L. Karlsson, B. Wannberg, G. Öhrwall, D. M. P. Holland, M. A. MacDonald, M. A. Hayes, and W. von Niessen, *Chem. Phys.* **224**, 95 (1997)]; See also H.-G. Weikert and L. S. Cederbaum, *Chem. Phys. Lett.* **237**, 1 (1995).
- ⁶³H. Müller, H. Köppel, and L. S. Cederbaum, *New J. Chem.* **17**, 7 (1993).
- ⁶⁴K. R. Asmis, T. R. Taylor, and D. M. Neumark, *J. Chem. Phys.* **111**, 8838 (1999).
- ⁶⁵T. Ichino, J. F. Stanton, and J. Gauss (unpublished).
- ⁶⁶That is, the determination of the LJT coupling constant, which is usually done by evaluating the first derivative of the adiabatic potential energy along the mode of interest, could also, in principle, be done by calculating the interstate coupling constant between the two components of the degenerate state. These are—apart from phase considerations—precisely equal [see Eq. (2)], and the check alluded to in the text demonstrates that the method used in the analytic λ calculation is entirely consistent in the sense that this condition is obeyed.
- ⁶⁷The PJT interactions with the \tilde{B} and \tilde{E}^2E_2' states constructively interfere, and significant enhancement of the intensity of the peak for the fundamental level of the e_1'' mode is predicted by the simulation. See also discussion given in EPAPS (Ref. 43).
- ⁶⁸Relative intensities should be assessed in the magic angle spectrum where intensities are free from β dependence [see Eq. (1)].
- ⁶⁹The assumption of equal cross sections for detachment to all the electronic states leaves some uncertainties with respect to the relative intensities of the nonadiabatic peaks. For example, quite a large disparity in the magnitude of photodetachment cross sections has been found for different electronic states of NO_3 radical; see A. Weaver, D. W. Arnold, S. E. Bradforth, and D. M. Neumark, *J. Chem. Phys.* **94**, 1740 (1991) and Ref. 54.
- ⁷⁰K. J. Reed, A. H. Zimmerman, H. C. Andersen, and J. I. Brauman, *J. Chem. Phys.* **64**, 1368 (1976).
- ⁷¹More rigorous arguments should consider, for instance, $\Delta l = +1$ processes, its associated interference effects along with phase shifts, and the photoelectron momentum dependence.
- ⁷²The distinct β values for the $J = \pm 1/2$ and $\pm 3/2$ vibronic levels observed in the photoelectron spectrum of CH_3O^- (see Refs. 57 and 58) can be rationalized in the same way.
- ⁷³J. Eiding, R. Schneider, W. Domcke, H. Köppel, and W. von Niessen, *Chem. Phys. Lett.* **177**, 345 (1991); **191**, 203 (1992).
- ⁷⁴The Green's function methods long applied to this problem by the Heidelberg group are—like EOMIP-CC—extremely well-suited to the study of nonadiabaticity. Indeed, both are based on a closed-shell reference state that contains one electron more than the target state and exploit the mathematical structure of Fock space to achieve balance in the description of the target states as well as to obey appropriate spin and spatial symmetry constraints.
- ⁷⁵The fundamental level of an a_{1g} mode (ν_2 , ring-breathing) is located not in the very vicinity of the vibronic levels of $J = \pm 1/2$ in \tilde{X}^2E_{1g} $C_6H_6^+$. See Ref. 73.
- ⁷⁶U. Höper, P. Botschwina, and H. Köppel, *J. Chem. Phys.* **112**, 4132 (2000).
- ⁷⁷J. Schmidt-Klügmann, H. Köppel, S. Schmatz, and P. Botschwina, *Chem. Phys. Lett.* **369**, 21 (2003).
- ⁷⁸M. H. Perrin and M. Gouterman, *J. Chem. Phys.* **46**, 1019 (1967).
- ⁷⁹J. H. van der Waals, A. M. D. Berghuis, and M. S. de Groot, *Mol. Phys.* **13**, 301 (1967).
- ⁸⁰M. Z. Zgierski and M. Pawlikowski, *J. Chem. Phys.* **70**, 3444 (1979).
- ⁸¹E. Haller, H. Köppel, L. S. Cederbaum, W. von Niessen, and G. Bieri, *J. Chem. Phys.* **78**, 1359 (1983).
- ⁸²H. Köppel, L. S. Cederbaum, and W. Domcke, *J. Chem. Phys.* **89**, 2023 (1988).
- ⁸³S. Mahapatra, G. A. Worth, H.-D. Meyer, L. S. Cederbaum, and H. Köppel, *J. Phys. Chem. A* **105**, 5567 (2001).
- ⁸⁴M. Döscher, H. Köppel, and P. G. Szalay, *J. Chem. Phys.* **117**, 2645 (2002).
- ⁸⁵H. Köppel, M. Döscher, I. Bâldea, H.-D. Meyer, and P. G. Szalay, *J. Chem. Phys.* **117**, 2657 (2002).
- ⁸⁶W. Eisfeld and A. Viel, *J. Chem. Phys.* **122**, 204317 (2005).
- ⁸⁷T. Sears, T. A. Miller, and V. E. Bondybey, *J. Chem. Phys.* **72**, 6070 (1980).
- ⁸⁸E. Haller, L. S. Cederbaum, and W. Domcke, *Mol. Phys.* **41**, 1291 (1980).
- ⁸⁹T. A. Barckholtz and T. A. Miller, *Int. Rev. Phys. Chem.* **17**, 435 (1998).
- ⁹⁰The EOMIP-CCSD/DZP calculations yield a Jahn–Teller stabilization energy of 0.187 eV.
- ⁹¹This finding highlights a strength of the EOMIP-CCSD method. While the choice of active space in multiconfiguration calculations such as those of Refs. 26 and 27 is guided by those states believed to be important, EOMIP-CCSD is effectively a black-box method in the current application. If one wanted to include PJT effects in a CASSCF study, then this would certainly influence the choice of active space. However, in EOMIP-CCSD, these effects appear automatically. See Ref. 33 for an advanced discussion of EOMIP-CCSD in the context of vibronic coupling.
- ⁹²T. Ichino and J. F. Stanton (unpublished).
- ⁹³H. Richter and J. B. Howard, *Prog. Energy Combust. Sci.* **26**, 565 (2000).
- ⁹⁴M. Frenklach, *Phys. Chem. Chem. Phys.* **4**, 2028 (2002).
- ⁹⁵J. A. Miller, M. J. Pilling, and J. Troe, *Proc. Combust. Inst.* **30**, 43 (2005).
- ⁹⁶C. S. McEnally, L. D. Pfefferle, B. Atakan, and K. Kohse-Hoinghaus, *Prog. Energy Combust. Sci.* **32**, 247 (2006).
- ⁹⁷N. M. Marinov, W. J. Pitz, C. K. Westbrook, M. J. Castaldi, and S. M. Senkan, *Combust. Sci. Technol.* **116**, 211 (1996).
- ⁹⁸C. F. Melius, M. E. Colvin, N. M. Marinov, W. J. Pitz, and S. M. Senkan, *Proc. Combust. Inst.* **26**, 685 (1996).
- ⁹⁹L. V. Moskaleva, A. M. Mebel, and M. C. Lin, *Proc. Combust. Inst.* **26**, 521 (1996).
- ¹⁰⁰E. Ikeda, R. S. Tranter, J. H. Kiefer, R. D. Kern, H. J. Singh, and Q. Zhang, *Proc. Combust. Inst.* **28**, 1725 (2000).
- ¹⁰¹J. D. Bittner and J. B. Howard, *Proc. Combust. Inst.* **18**, 1105 (1981).
- ¹⁰²C. Venkat, K. Brezinsky, and I. Glassman, *Proc. Combust. Inst.* **19**, 143 (1982).
- ¹⁰³K. Brezinsky, *Prog. Energy Combust. Sci.* **12**, 1 (1986).
- ¹⁰⁴B. K. Carpenter, *J. Am. Chem. Soc.* **115**, 9806 (1993).
- ¹⁰⁵T. Yu and M. C. Lin, *J. Am. Chem. Soc.* **116**, 9571 (1994).
- ¹⁰⁶C. Barckholtz, M. J. Fadden, and C. M. Hadad, *J. Phys. Chem. A* **103**, 8108 (1999).
- ¹⁰⁷M. J. Fadden, C. Barckholtz, and C. M. Hadad, *J. Phys. Chem. A* **104**, 3004 (2000).
- ¹⁰⁸C. Barckholtz, T. A. Barckholtz, and C. M. Hadad, *J. Phys. Chem. A* **105**, 140 (2001).
- ¹⁰⁹S. M. Kroner, M. P. DeMatteo, C. M. Hadad, and B. K. Carpenter, *J. Am. Chem. Soc.* **127**, 7466 (2005).
- ¹¹⁰S. Furuyama, D. M. Golden, and S. W. Benson, *J. Chem. Thermodyn.* **2**, 161 (1970).
- ¹¹¹D. J. DeFrees, R. T. McIver, Jr., and W. J. Hehre, *J. Am. Chem. Soc.* **102**, 3334 (1980).
- ¹¹²R. D. Kern, Q. Zhang, J. Yao, B. S. Jursic, R. S. Tranter, M. A. Greybill, and J. H. Kiefer, *Proc. Combust. Inst.* **27**, 143 (1998).
- ¹¹³K. Roy, C. Horn, P. Frank, V. G. Slutsky, and T. Just, *Proc. Combust. Inst.* **27**, 329 (1998).
- ¹¹⁴K. Roy, M. Braun-Unkhoff, P. Frank, and T. Just, *Int. J. Chem. Kinet.* **33**, 821 (2001).
- ¹¹⁵P. M. Nunes, F. Agapito, B. J. C. Cabral, R. M. B. dos Santos, and J. A. M. Simões, *J. Phys. Chem. A* **110**, 5130 (2006).
- ¹¹⁶J. Berkowitz, G. B. Ellison, and D. Gutman, *J. Phys. Chem.* **98**, 2744

(1994).

¹¹⁷J. E. Bartmess, in *NIST Chemistry Webbook*, NIST Standard Reference Database No. 69, edited by J. P. Linstrom and W. G. Mallard (National Institute of Standards and Technology, Gaithersburg, MD, 2005).

¹¹⁸J. E. Bartmess, J. A. Scott, and R. T. McIver, Jr., *J. Am. Chem. Soc.* **101**, 6046 (1979).

¹¹⁹M. W. Chase, Jr., *NIST-JANAF Thermochemical Tables*, 4th ed. (American Chemical Society, Washington, DC, 1998).